EUROPEAN ORGANIZATION FOR NUCLEAR RESEARCH (CERN)

CERN-LHCC-2021-002
LHCb-TDR-022
May 4, 2021

LHCb PLUME: Probe for LUminosity MEasurement

LHCb collaboration

Contents

LHCb collaboration

R. Aaij[32], C. Abellán Beteta[50], T. Ackernley[60], B. Adeva[46], M. Adinolfi[54], H. Afsharnia[9], C.A. Aidala[85], S. Aiola[25], Z. Ajaltouni[9], S. Akar[65], J. Albrecht[15], F. Alessio[48], M. Alexander[59], A. Alfonso Albero[45], Z. Aliouche[62], G. Alkhazov[38], P. Alvarez Cartelle[55], S. Amato[2], Y. Amhis[11], L. An[48], L. Anderlini[22], A. Andreianov[38], M. Andreotti[21], F. Archilli[17], A. Artamonov[44], M. Artuso[68], K. Arzymatov[42], E. Aslanides[10], M. Atzeni[50], B. Audurier[12], S. Bachmann[17], M. Bachmayer[49], J.J. Back[56], P. Baladron Rodriguez[46], V. Balagura[12], G. Balbi[20], W. Baldini[21], J. Baptista Leite[1], R.J. Barlow[62], S. Barsuk[11], W. Barter[61], M. Bartolini[24], F. Baryshnikov[82], J.M. Basels[14], G. Bassi[29], B. Batsukh[68], A. Battig[15], A. Bay[49], M. Becker[15], F. Bedeschi[29], I. Bediaga[1], C. Beigbeder[11], A. Beiter[68], V. Belavin[42], S. Belin[27], V. Bellee[49], K. Belous[44], I. Belov[40], I. Belyaev[41], G. Bencivenni[23], E. Ben-Haim[13], A. Berezhnoy[40], F. Bernard[49], R. Bernet[50], D. Berninghoff[17], H.C. Bernstein[68], C. Bertella[48], A. Bertolin[28], C. Betancourt[50], F. Betti[48], Ia. Bezshyiko[50], O. Bezshyyko[86], S. Bhasin[54], J. Bhom[35], L. Bian[73], M.S. Bieker[15], S. Bifani[53], P. Billoir[13], M. Birch[61], F.C.R. Bishop[55], A. Bitadze[62], A. Bizzeti[22,k], M. Bjørn[63], M.P. Blago[48], T. Blake[56], F. Blanc[49], S. Blusk[68], D. Bobulska[59], J.A. Boelhauve[15], O. Boente Garcia[46], T. Boettcher[64], I. Boiaryntseva[87], A. Boldyrev[81], A. Bondar[43], N. Bondar[38,48], S. Borghi[62], M. Borisyak[42], M. Borsato[17], J.T. Borsuk[35], S.A. Bouchiba[49], T.J.V. Bowcock[60], A. Boyaryntsev[87], A. Boyer[48], C. Bozzi[21], M.J. Bradley[61], S. Braun[66], A. Brea Rodriguez[46], M. Briere[11], M. Brodski[48], J. Brodzicka[35], A. Brossa Gonzalo[56], D. Brundu[27], A. Buonaura[50], L. Burmistrov[11], C. Burr[48], A. Bursche[72], A. Butkevich[39], J.S. Butter[32], J. Buytaert[48], W. Byczynski[48], S. Cadeddu[27], H. Cai[73], R. Calabrese[21,f], L. Calefice[15,13], L. Calero Diaz[23], S. Cali[23], R. Calladine[53], M. Calvi[26,j], M. Calvo Gomez[84], P. Camargo Magalhaes[54], A. Camboni[45,84], P. Campana[23], A.F. Campoverde Quezada[6], S. Capelli[26,j], L. Capriotti[20,d], A. Carbone[20,d], G. Carboni[31], R. Cardinale[24], A. Cardini[27], I. Carli[4], P. Carniti[26,j], L. Carus[14], K. Carvalho Akiba[32], A. Casais Vidal[46], G. Casse[60], M. Cattaneo[48], G. Cavallero[48], S. Celani[49], J. Cerasoli[10], A.J. Chadwick[60], X. Chang[48], M.G. Chapman[54], M. Charles[13], Ph. Charpentier[48], G. Chatzikonstantinidis[53], V. Chaumat[11], C.A. Chavez Barajas[60], M. Chefdeville[8], C. Chen[3], S. Chen[4], A. Chernov[35], V. Chobanova[46], S. Cholak[49], M. Chrzaszcz[35], A. Chubykin[38], V. Chulikov[38], P. Ciambrone[23], M.F. Cicala[56], X. Cid Vidal[46], G. Ciezarek[48], P.E.L. Clarke[58], M. Clemencic[48], H.V. Cliff[55], J. Closier[48], J.L. Cobbledick[62], V. Coco[48], J.A.B. Coelho[11], J. Cogan[10], E. Cogneras[9], L. Cojocariu[37], P. Collins[48], T. Colombo[48], L. Congedo[19,c], A. Contu[27], N. Cooke[53], G. Coombs[59], G. Corti[48], C.M. Costa Sobral[56], B. Couturier[48], D.C. Craik[64], J. Crkovská[67], M. Cruz Torres[1], R. Currie[58], C.L. Da Silva[67], E. Dall'Occo[15], J. Dalseno[46], C. D'Ambrosio[48], A. Danilina[41], P. d'Argent[48], A. Davis[62], O. De Aguiar Francisco[62], K. De Bruyn[78], S. De Capua[62], M. De Cian[49], J.M. De Miranda[1], L. De Paula[2], M. De Serio[19,c], D. De Simone[50], P. De Simone[23], J.A. de Vries[79], C.T. Dean[67], D. Decamp[8], L. Del Buono[13], B. Delaney[55], H.-P. Dembinski[15], A. Dendek[34], V. Denysenko[50], D. Derkach[81], O. Deschamps[9], F. Desse[11], F. Dettori[27,e], B. Dey[73], P. Di Nezza[23], S. Didenko[82], L. Dieste Maronas[46], H. Dijkstra[48], V. Dobishuk[52], A.M. Donohoe[18], F. Dordei[27], A.C. dos Reis[1], L. Douglas[59], A. Dovbnya[51], A.G. Downes[8], K. Dreimanis[60], O. Duarte[11], M.W. Dudek[35], L. Dufour[48], V. Duk[77], P. Durante[48], J.M. Durham[67], D. Dutta[62], A. Dziurda[35], A. Dzyuba[38], S. Easo[57], U. Egede[69], V. Egorychev[41], S. Eidelman[43,v], S. Eisenhardt[58], S. Ek-In[49], L. Eklund[59,w], S. Ely[68], A. Ene[37], E. Epple[67], S. Escher[14], J. Eschle[50], S. Esen[13], T. Evans[48], A. Falabella[20], J. Fan[3], Y. Fan[6], B. Fang[73], S. Farry[60], D. Fazzini[26,j], M. Féo[48], A. Fernandez Prieto[46], J.M. Fernandez-tenllado Arribas[45], A.D. Fernez[66], F. Ferrari[20,d], L. Ferreira Lopes[49], F. Ferreira Rodrigues[2], S. Ferreres Sole[32], M. Ferrillo[50], M. Ferro-Luzzi[48], S. Filippov[39], R.A. Fini[19], M. Fiorini[21,f], M. Firlej[34], K.M. Fischer[63], D. Fitzgerald[85], C. Fitzpatrick[62], T. Fiutowski[34], F. Fleuret[12], M. Fontana[13],

F. Fontanelli[24,h], R. Forty[48], V. Franco Lima[60], M. Franco Sevilla[66], M. Frank[48], E. Franzoso[21], G. Frau[17], C. Frei[48], R. Frei[48], D.A. Friday[59], J. Fu[25], Q. Fuehring[15], W. Funk[48], E. Gabriel[32], T. Gaintseva[42], A. Gallas Torreira[46], D. Galli[20,d], S. Gambetta[58,48], Y. Gan[3], M. Gandelman[2], P. Gandini[25], Y. Gao[5], M. Garau[27], L.M. Garcia Martin[56], P. Garcia Moreno[45], J. García Pardiñas[26,j], B. Garcia Plana[46], F.A. Garcia Rosales[12], L. Garrido[45], C. Gaspar[48], R.E. Geertsema[32], D. Gerick[17], L.L. Gerken[15], E. Gersabeck[62], M. Gersabeck[62], T. Gershon[56], D. Gerstel[10], Ph. Ghez[8], V. Gibson[55], H.K. Giemza[36], M. Giovannetti[23,p], A. Gioventù[46], P. Gironella Gironell[45], L. Giubega[37], C. Giugliano[21,f,48], K. Gizdov[58], E.L. Gkougkousis[48], V.V. Gligorov[13], C. Göbel[70], L. Golinka-Bezshyyko[86], E. Golobardes[84], D. Golubkov[41], A. Golutvin[61,82], A. Gomes[1,a], S. Gomez Fernandez[45], F. Goncalves Abrantes[63], M. Goncerz[35], G. Gong[3], P. Gorbounov[41], I.V. Gorelov[40], C. Gotti[26], E. Govorkova[48], J.P. Grabowski[17], T. Grammatico[13], L.A. Granado Cardoso[48], E. Graugés[45], E. Graverini[49], G. Graziani[22], A. Grecu[37], L.M. Greeven[32], P. Griffith[21,f], L. Grillo[62], S. Gromov[82], B.R. Gruberg Cazon[63], B. Grynyov[87], C. Gu[3], M. Guarise[21], P. A. Günther[17], E. Gushchin[39], A. Guth[14], Y. Guz[44], T. Gys[48], T. Hadavizadeh[69], G. Haefeli[49], C. Haen[48], J. Haimberger[48], T. Halewood-leagas[60], P.M. Hamilton[66], J.P. Hammerich[60], Q. Han[7], X. Han[17], T.H. Hancock[63], S. Hansmann-Menzemer[17], N. Harnew[63], T. Harrison[60], C. Hasse[48], M. Hatch[48], J. He[6,b], M. Hecker[61], K. Heijhoff[32], K. Heinicke[15], A.M. Hennequin[48], K. Hennessy[60], L. Henry[25,47], J. Heuel[14], A. Hicheur[2], D. Hill[49], M. Hilton[62], S.E. Hollitt[15], J. Hu[17], J. Hu[72], W. Hu[7], W. Huang[6], X. Huang[73], W. Hulsbergen[32], R.J. Hunter[56], M. Hushchyn[81], D. Hutchcroft[60], D. Hynds[32], P. Ibis[15], M. Idzik[34], D. Ilin[38], P. Ilten[65], A. Inglessi[38], A. Ishteev[82], K. Ivshin[38], R. Jacobsson[48], S. Jakobsen[48], E. Jans[32], B.K. Jashal[47], A. Jawahery[66], V. Jevtic[15], M. Jezabek[35], F. Jiang[3], M. John[63], D. Johnson[48], C.R. Jones[55], T.P. Jones[56], B. Jost[48], N. Jurik[48], S. Kandybei[51], Y. Kang[3], M. Karacson[48], M. Karpov[81], F. Keizer[55,48], M. Kenzie[56], T. Ketel[33], B. Khanji[15], A. Kharisova[83], S. Kholodenko[44], T. Kirn[14], V.S. Kirsebom[49], O. Kitouni[64], S. Klaver[32], K. Klimaszewski[36], S. Koliiev[52], A. Kondybayeva[82], A. Konoplyannikov[41], P. Kopciewicz[34], R. Kopecna[17], P. Koppenburg[32], M. Korolev[40], I. Kostiuk[32,52], O. Kot[52], S. Kotriakhova[21,38], P. Kravchenko[38], L. Kravchuk[39], R.D. Krawczyk[48], M. Kreps[56], F. Kress[61], S. Kretzschmar[14], P. Krokovny[43,v], W. Krupa[34], W. Krzemien[36], W. Kucewicz[35,t], M. Kucharczyk[35], V. Kudryavtsev[43,v], H.S. Kuindersma[32], G.J. Kunde[67], V. Kushnir[51], T. Kvaratskheliya[41], D. Lacarrere[48], G. Lafferty[62], A. Lai[27], A. Lampis[27], D. Lancierini[50], J.J. Lane[62], R. Lane[54], G. Lanfranchi[23], C. Langenbruch[14], J. Langer[15], O. Lantwin[50], T. Latham[56], F. Lazzari[29,q], R. Le Gac[10], S.H. Lee[85], R. Lefèvre[9], A. Leflat[40], S. Legotin[82], O. Leroy[10], T. Lesiak[35], B. Leverington[17], H. Li[72], L. Li[63], P. Li[17], S. Li[7], Y. Li[4], Y. Li[4], Z. Li[68], X. Liang[68], T. Lin[61], R. Lindner[48], V. Lisovskyi[15], R. Litvinov[27], G. Liu[72], H. Liu[6], S. Liu[4], X. Liu[3], A. Loi[27], J. Lomba Castro[46], I. Longstaff[59], J.H. Lopes[2], G.H. Lovell[55], Y. Lu[4], D. Lucchesi[28,l], S. Luchuk[39], M. Lucio Martinez[32], V. Lukashenko[32], Y. Luo[3], A. Lupato[62], E. Luppi[21,f], O. Lupton[56], A. Lusiani[29,m], X. Lyu[6], L. Ma[4], R. Ma[6], S. Maccolini[20,d], F. Machefert[11], F. Maciuc[37], V. Macko[49], P. Mackowiak[15], S. Maddrell-Mander[54], O. Madejczyk[34], L.R. Madhan Mohan[54], O. Maev[38], A. Maevskiy[81], D. Maisuzenko[38], M.W. Majewski[34], J.J. Malczewski[35], S. Malde[63], B. Malecki[48], A. Malinin[80], T. Maltsev[43,v], H. Malygina[17], G. Manca[27,e], G. Mancinelli[10], D. Manuzzi[20,d], D. Marangotto[25,i], J. Maratas[9,s], J.F. Marchand[8], U. Marconi[20], S. Mariani[22,g], C. Marin Benito[48], M. Marinangeli[49], J. Marks[17], A.M. Marshall[54], P.J. Marshall[60], G. Martellotti[30], L. Martinazzoli[48,j], M. Martinelli[26,j], D. Martinez Santos[46], F. Martinez Vidal[47], A. Massafferri[1], M. Materok[14], R. Matev[48], A. Mathad[50], Z. Mathe[48], V. Matiunin[41], C. Matteuzzi[26], K.R. Mattioli[85], A. Mauri[32], E. Maurice[12], J. Mauricio[45], M. Mazurek[36], M. McCann[61], L. Mcconnell[18], T.H. Mcgrath[62], A. McNab[62], R. McNulty[18], J.V. Mead[60], B. Meadows[65], C. Meaux[10], G. Meier[15], N. Meinert[76], D. Melnychuk[36], S. Meloni[26,j], M. Merk[32,79], A. Merli[25], L. Meyer Garcia[2], M. Mikhasenko[48], D.A. Milanes[74],

E. Millard[56], M. Milovanovic[48], M.-N. Minard[8], A. Minotti[21], L. Minzoni[21,f], S.E. Mitchell[58], B. Mitreska[62], D.S. Mitzel[48], A. Mödden [15], R.A. Mohammed[63], R.D. Moise[61], T. Mombächer[15], I.A. Monroy[74], S. Monteil[9], M. Morandin[28], G. Morello[23], M.J. Morello[29,m], J. Moron[34], A.B. Morris[75], A.G. Morris[56], R. Mountain[68], H. Mu[3], F. Muheim[58,48], M. Mulder[48], D. Müller[48], K. Müller[50], C.H. Murphy[63], D. Murray[62], P. Muzzetto[27,48], V. Mytrochenko[51], P. Naik[54], T. Nakada[49], R. Nandakumar[57], T. Nanut[49], I. Nasteva[2], M. Needham[58], T. Nepokupna[87], I. Neri[21], N. Neri[25,i], S. Neubert[75], N. Neufeld[48], R. Newcombe[61], T.D. Nguyen[49], C. Nguyen-Mau[49,x], E.M. Niel[11], S. Nieswand[14], N. Nikitin[40], N.S. Nolte[15], C. Nunez[85], A. Oblakowska-Mucha[34], V. Obraztsov[44], D.P. O'Hanlon[54], R. Oldeman[27,e], M.E. Olivares[68], C.J.G. Onderwater[78], V. Orlov[86], A. Ossowska[35], J.M. Otalora Goicochea[2], T. Ovsiannikova[41], P. Owen[50], A. Oyanguren[47], B. Pagare[56], P.R. Pais[48], T. Pajero[63], A. Palano[19], M. Palutan[23], Y. Pan[62], G. Panshin[83], A. Papanestis[57], M. Pappagallo[19,c], L.L. Pappalardo[21,f], C. Pappenheimer[65], W. Parker[66], C. Parkes[62], C.J. Parkinson[46], B. Passalacqua[21], G. Passaleva[22], A. Pastore[19], M. Patel[61], C. Patrignani[20,d], C.J. Pawley[79], A. Pearce[48], A. Pellegrino[32], M. Pepe Altarelli[48], S. Perazzini[20], D. Pereima[41], S. Perezhogin[51], P. Perret[9], M. Petric[59,48], K. Petridis[54], A. Petrolini[24,h], A. Petrov[80], S. Petrucci[58], M. Petruzzo[25], T.T.H. Pham[68], A. Philippov[42], L. Pica[29,n], M. Piccini[77], B. Pietrzyk[8], G. Pietrzyk[49], M. Pili[63], D. Pinci[30], F. Pisani[48], Resmi P.K[10], V. Placinta[37], J. Plews[53], M. Plo Casasus[46], F. Polci[13], M. Poli Lener[23], M. Poliakova[68], A. Poluektov[10], N. Polukhina[82,u], I. Polyakov[68], E. Polycarpo[2], G.J. Pomery[54], S. Ponce[48], D. Popov[6,48], S. Popov[42], S. Poslavskii[44], K. Prasanth[35], L. Promberger[48], C. Prouve[46], V. Pugatch[52], V. Puill[11], H. Pullen[63], G. Punzi[29,n], W. Qian[6], J. Qin[6], R. Quagliani[13], B. Quintana[8], N.V. Raab[18], R.I. Rabadan Trejo[10], B. Rachwal[34], J.H. Rademacker[54], M. Rama[29], M. Ramos Pernas[56], M.S. Rangel[2], F. Ratnikov[42,81], G. Raven[33], M. Reboud[8], F. Redi[49], F. Reiss[62], C. Remon Alepuz[47], Z. Ren[3], V. Renaudin[63], R. Ribatti[29], S. Ricciardi[57], K. Rinnert[60], P. Robbe[11], G. Robertson[58], J. Rochet[48], A.B. Rodrigues[49], E. Rodrigues[60], J.A. Rodriguez Lopez[74], A. Rollings[63], P. Roloff[48], V. Romanovskiy[44], M. Romero Lamas[46], A. Romero Vidal[46], J.D. Roth[85], M. Rotondo[23], L. Roy[48], M.S. Rudolph[68], T. Ruf[48], J. Ruiz Vidal[47], A. Ryzhikov[81], J. Ryzka[34], J.J. Saborido Silva[46], N. Sagidova[38], N. Sahoo[56], B. Saitta[27,e], M. Salomoni[48], D. Sanchez Gonzalo[45], C. Sanchez Gras[32], F. Sanders[32,48], R. Santacesaria[30], C. Santamarina Rios[46], M. Santimaria[23], E. Santovetti[31,p], D. Saranin[82], G. Sarpis[59], M. Sarpis[75], A. Sarti[30], C. Satriano[30,o], A. Satta[31], M. Saur[15], D. Savrina[41,40], H. Sazak[9], L.G. Scantlebury Smead[63], S. Schael[14], M. Schellenberg[15], M. Schiller[59], H. Schindler[48], M. Schmelling[16], B. Schmidt[48], O. Schneider[49], A. Schopper[48], M. Schubiger[32], S. Schulte[49], M.H. Schune[11], R. Schwemmer[48], B. Sciascia[23], S. Sellam[46], A. Semennikov[41], M. Senghi Soares[33], A. Sergi[24], N. Serra[50], L. Sestini[28], A. Seuthe[15], P. Seyfert[48], Y. Shang[5], D.M. Shangase[85], M. Shapkin[44], I. Shchemerov[82], L. Shchutska[49], T. Shears[60], L. Shekhtman[43,v], Z. Shen[5], V. Shevchenko[80], E.B. Shields[26,j], E. Shmanin[82], J.D. Shupperd[68], B.G. Siddi[21], R. Silva Coutinho[50], G. Simi[28], S. Simone[19,c], N. Skidmore[62], T. Skwarnicki[68], M.W. Slater[53], I. Slazyk[21,f], J.C. Smallwood[63], J.G. Smeaton[55], A. Smetkina[41], E. Smith[14], M. Smith[61], A. Snoch[32], M. Soares[20], L. Soares Lavra[9], M.D. Sokoloff[65], F.J.P. Soler[59], A. Solovev[38], I. Solovyev[38], F.L. Souza De Almeida[2], B. Souza De Paula[2], B. Spaan[15], E. Spadaro Norella[25,i], P. Spradlin[59], F. Stagni[48], M. Stahl[65], S. Stahl[48], P. Stefko[49], O. Steinkamp[50,82], O. Stenyakin[44], H. Stevens[15], S. Stone[68], M.E. Stramaglia[49], M. Straticiuc[37], D. Strekalina[82], F. Suljik[63], J. Sun[27], L. Sun[73], Y. Sun[66], P. Svihra[62], P.N. Swallow[53], K. Swientek[34], A. Szabelski[36], T. Szumlak[34], M. Szymanski[48], S. Taneja[62], F. Teubert[48], E. Thomas[48], K.A. Thomson[60], V. Tisserand[9], S. T'Jampens[8], M. Tobin[4], L. Tomassetti[21,f], D. Torres Machado[1], D.Y. Tou[13], M.T. Tran[49], E. Trifonova[82], C. Trippl[49], T.N. Trung[11], G. Tuci[29,n], A. Tully[49], N. Tuning[32,48], A. Ukleja[36], D.J. Unverzagt[17], E. Ursov[82], A. Usachov[32], A. Ustyuzhanin[42,81], U. Uwer[17], A. Vagner[83], V. Vagnoni[20], A. Valassi[48], G. Valenti[20],

N. Valls Canudas[84], M. van Beuzekom[32], M. Van Dijk[49], E. van Herwijnen[82], C.B. Van Hulse[18], M. van Veghel[78], R. Vazquez Gomez[46], P. Vazquez Regueiro[46], C. Vázquez Sierra[48], S. Vecchi[21], J.J. Velthuis[54], M. Veltri[22,r], A. Venkateswaran[68], M. Veronesi[32], M. Vesterinen[56], D. Vieira[65], M. Vieites Diaz[49], H. Viemann[76], X. Vilasis-Cardona[84], E. Vilella Figueras[60], A. Villa[20,d], P. Vincent[13], D. Vom Bruch[10], A. Vorobyev[38], V. Vorobyev[43,v], N. Voropaev[38], R. Waldi[76], J. Walsh[29], C. Wang[17], J. Wang[5], J. Wang[4], J. Wang[3], J. Wang[73], M. Wang[3], R. Wang[54], Y. Wang[7], Z. Wang[50], Z. Wang[3], H.M. Wark[60], N.K. Watson[53], S.G. Weber[13], D. Websdale[61], C. Weisser[64], B.D.C. Westhenry[54], D.J. White[62], M. Whitehead[54], D. Wiedner[15], G. Wilkinson[63], M. Wilkinson[68], I. Williams[55], M. Williams[64], M.R.J. Williams[58], F.F. Wilson[57], W. Wislicki[36], M. Witek[35], L. Witola[17], G. Wormser[11], S.A. Wotton[55], H. Wu[68], K. Wyllie[48], Z. Xiang[6], D. Xiao[7], Y. Xie[7], A. Xu[5], J. Xu[6], L. Xu[3], M. Xu[7], Q. Xu[6], Z. Xu[5], Z. Xu[6], D. Yang[3], S. Yang[6], Y. Yang[6], Z. Yang[3], Z. Yang[66], Y. Yao[68], L.E. Yeomans[60], V. Yeroshenko[86], H. Yin[7], J. Yu[71], X. Yuan[68], O. Yushchenko[44], E. Zaffaroni[49], M. Zavertyaev[16,u], M. Zdybal[35], O. Zenaiev[48], M. Zeng[3], D. Zhang[7], L. Zhang[3], S. Zhang[5], Y. Zhang[5], Y. Zhang[63], A. Zhelezov[17], Y. Zheng[6], X. Zhou[6], Y. Zhou[6], X. Zhu[3], Z. Zhu[6], V. Zhukov[14,40], J.B. Zonneveld[58], Q. Zou[4], S. Zucchelli[20,d], D. Zuliani[28], G. Zunica[62].

[1] *Centro Brasileiro de Pesquisas Físicas (CBPF), Rio de Janeiro, Brazil*
[2] *Universidade Federal do Rio de Janeiro (UFRJ), Rio de Janeiro, Brazil*
[3] *Center for High Energy Physics, Tsinghua University, Beijing, China*
[4] *Institute Of High Energy Physics (IHEP), Beijing, China*
[5] *School of Physics State Key Laboratory of Nuclear Physics and Technology, Peking University, Beijing, China*
[6] *University of Chinese Academy of Sciences, Beijing, China*
[7] *Institute of Particle Physics, Central China Normal University, Wuhan, Hubei, China*
[8] *Univ. Grenoble Alpes, Univ. Savoie Mont Blanc, CNRS, IN2P3-LAPP, Annecy, France*
[9] *Université Clermont Auvergne, CNRS/IN2P3, LPC, Clermont-Ferrand, France*
[10] *Aix Marseille Univ, CNRS/IN2P3, CPPM, Marseille, France*
[11] *Université Paris-Saclay, CNRS/IN2P3, IJCLab, Orsay, France*
[12] *Laboratoire Leprince-Ringuet, CNRS/IN2P3, Ecole Polytechnique, Institut Polytechnique de Paris, Palaiseau, France*
[13] *LPNHE, Sorbonne Université, Paris Diderot Sorbonne Paris Cité, CNRS/IN2P3, Paris, France*
[14] *I. Physikalisches Institut, RWTH Aachen University, Aachen, Germany*
[15] *Fakultät Physik, Technische Universität Dortmund, Dortmund, Germany*
[16] *Max-Planck-Institut für Kernphysik (MPIK), Heidelberg, Germany*
[17] *Physikalisches Institut, Ruprecht-Karls-Universität Heidelberg, Heidelberg, Germany*
[18] *School of Physics, University College Dublin, Dublin, Ireland*
[19] *INFN Sezione di Bari, Bari, Italy*
[20] *INFN Sezione di Bologna, Bologna, Italy*
[21] *INFN Sezione di Ferrara, Ferrara, Italy*
[22] *INFN Sezione di Firenze, Firenze, Italy*
[23] *INFN Laboratori Nazionali di Frascati, Frascati, Italy*
[24] *INFN Sezione di Genova, Genova, Italy*
[25] *INFN Sezione di Milano, Milano, Italy*
[26] *INFN Sezione di Milano-Bicocca, Milano, Italy*
[27] *INFN Sezione di Cagliari, Monserrato, Italy*
[28] *Universita degli Studi di Padova, Universita e INFN, Padova, Padova, Italy*
[29] *INFN Sezione di Pisa, Pisa, Italy*
[30] *INFN Sezione di Roma La Sapienza, Roma, Italy*
[31] *INFN Sezione di Roma Tor Vergata, Roma, Italy*
[32] *Nikhef National Institute for Subatomic Physics, Amsterdam, Netherlands*
[33] *Nikhef National Institute for Subatomic Physics and VU University Amsterdam, Amsterdam, Netherlands*
[34] *AGH - University of Science and Technology, Faculty of Physics and Applied Computer Science, Kraków, Poland*

[35] *Henryk Niewodniczanski Institute of Nuclear Physics Polish Academy of Sciences, Kraków, Poland*
[36] *National Center for Nuclear Research (NCBJ), Warsaw, Poland*
[37] *Horia Hulubei National Institute of Physics and Nuclear Engineering, Bucharest-Magurele, Romania*
[38] *Petersburg Nuclear Physics Institute NRC Kurchatov Institute (PNPI NRC KI), Gatchina, Russia*
[39] *Institute for Nuclear Research of the Russian Academy of Sciences (INR RAS), Moscow, Russia*
[40] *Institute of Nuclear Physics, Moscow State University (SINP MSU), Moscow, Russia*
[41] *Institute of Theoretical and Experimental Physics NRC Kurchatov Institute (ITEP NRC KI), Moscow, Russia*
[42] *Yandex School of Data Analysis, Moscow, Russia*
[43] *Budker Institute of Nuclear Physics (SB RAS), Novosibirsk, Russia*
[44] *Institute for High Energy Physics NRC Kurchatov Institute (IHEP NRC KI), Protvino, Russia, Protvino, Russia*
[45] *ICCUB, Universitat de Barcelona, Barcelona, Spain*
[46] *Instituto Galego de Física de Altas Enerxías (IGFAE), Universidade de Santiago de Compostela, Santiago de Compostela, Spain*
[47] *Instituto de Fisica Corpuscular, Centro Mixto Universidad de Valencia - CSIC, Valencia, Spain*
[48] *European Organization for Nuclear Research (CERN), Geneva, Switzerland*
[49] *Institute of Physics, Ecole Polytechnique Fédérale de Lausanne (EPFL), Lausanne, Switzerland*
[50] *Physik-Institut, Universität Zürich, Zürich, Switzerland*
[51] *NSC Kharkiv Institute of Physics and Technology (NSC KIPT), Kharkiv, Ukraine*
[52] *Institute for Nuclear Research of the National Academy of Sciences (KINR), Kyiv, Ukraine*
[53] *University of Birmingham, Birmingham, United Kingdom*
[54] *H.H. Wills Physics Laboratory, University of Bristol, Bristol, United Kingdom*
[55] *Cavendish Laboratory, University of Cambridge, Cambridge, United Kingdom*
[56] *Department of Physics, University of Warwick, Coventry, United Kingdom*
[57] *STFC Rutherford Appleton Laboratory, Didcot, United Kingdom*
[58] *School of Physics and Astronomy, University of Edinburgh, Edinburgh, United Kingdom*
[59] *School of Physics and Astronomy, University of Glasgow, Glasgow, United Kingdom*
[60] *Oliver Lodge Laboratory, University of Liverpool, Liverpool, United Kingdom*
[61] *Imperial College London, London, United Kingdom*
[62] *Department of Physics and Astronomy, University of Manchester, Manchester, United Kingdom*
[63] *Department of Physics, University of Oxford, Oxford, United Kingdom*
[64] *Massachusetts Institute of Technology, Cambridge, MA, United States*
[65] *University of Cincinnati, Cincinnati, OH, United States*
[66] *University of Maryland, College Park, MD, United States*
[67] *Los Alamos National Laboratory (LANL), Los Alamos, United States*
[68] *Syracuse University, Syracuse, NY, United States*
[69] *School of Physics and Astronomy, Monash University, Melbourne, Australia, associated to* [56]
[70] *Pontifícia Universidade Católica do Rio de Janeiro (PUC-Rio), Rio de Janeiro, Brazil, associated to* [2]
[71] *Physics and Micro Electronic College, Hunan University, Changsha City, China, associated to* [7]
[72] *Guangdong Provencial Key Laboratory of Nuclear Science, Institute of Quantum Matter, South China Normal University, Guangzhou, China, associated to* [3]
[73] *School of Physics and Technology, Wuhan University, Wuhan, China, associated to* [3]
[74] *Departamento de Fisica , Universidad Nacional de Colombia, Bogota, Colombia, associated to* [13]
[75] *Universität Bonn - Helmholtz-Institut für Strahlen und Kernphysik, Bonn, Germany, associated to* [17]
[76] *Institut für Physik, Universität Rostock, Rostock, Germany, associated to* [17]
[77] *INFN Sezione di Perugia, Perugia, Italy, associated to* [21]
[78] *Van Swinderen Institute, University of Groningen, Groningen, Netherlands, associated to* [32]
[79] *Universiteit Maastricht, Maastricht, Netherlands, associated to* [32]
[80] *National Research Centre Kurchatov Institute, Moscow, Russia, associated to* [41]
[81] *National Research University Higher School of Economics, Moscow, Russia, associated to* [42]
[82] *National University of Science and Technology "MISIS", Moscow, Russia, associated to* [41]
[83] *National Research Tomsk Polytechnic University, Tomsk, Russia, associated to* [41]
[84] *DS4DS, La Salle, Universitat Ramon Llull, Barcelona, Spain, associated to* [45]
[85] *University of Michigan, Ann Arbor, United States, associated to* [68]
[86] *Taras Shevchenko National University of Kyiv (TSNUK), Kyiv, Ukraine*

[87] *Institute for Scintillation Materials of National Academy of Sciences (ISMA), Kharkiv, Ukraine*

[a] *Universidade Federal do Triângulo Mineiro (UFTM), Uberaba-MG, Brazil*
[b] *Hangzhou Institute for Advanced Study, UCAS, Hangzhou, China*
[c] *Università di Bari, Bari, Italy*
[d] *Università di Bologna, Bologna, Italy*
[e] *Università di Cagliari, Cagliari, Italy*
[f] *Università di Ferrara, Ferrara, Italy*
[g] *Università di Firenze, Firenze, Italy*
[h] *Università di Genova, Genova, Italy*
[i] *Università degli Studi di Milano, Milano, Italy*
[j] *Università di Milano Bicocca, Milano, Italy*
[k] *Università di Modena e Reggio Emilia, Modena, Italy*
[l] *Università di Padova, Padova, Italy*
[m] *Scuola Normale Superiore, Pisa, Italy*
[n] *Università di Pisa, Pisa, Italy*
[o] *Università della Basilicata, Potenza, Italy*
[p] *Università di Roma Tor Vergata, Roma, Italy*
[q] *Università di Siena, Siena, Italy*
[r] *Università di Urbino, Urbino, Italy*
[s] *MSU - Iligan Institute of Technology (MSU-IIT), Iligan, Philippines*
[t] *AGH - University of Science and Technology, Faculty of Computer Science, Electronics and Telecommunications, Kraków, Poland*
[u] *P.N. Lebedev Physical Institute, Russian Academy of Science (LPI RAS), Moscow, Russia*
[v] *Novosibirsk State University, Novosibirsk, Russia*
[w] *Department of Physics and Astronomy, Uppsala University, Uppsala, Sweden*
[x] *Hanoi University of Science, Hanoi, Vietnam*

1 Introduction

During the operation in Run 1 and Run 2, from 2010 to 2018, the LHC beam was composed of a maximum of 2556 proton bunches, each with a population of 1.12×10^{11} protons. Such bunches collided at four beam interaction points (IPs) every 50 ns until 2016, and every 25 ns since then. Starting from 2022, the upgraded LHCb detector [1] will see during Run 3 a 5-fold increase of luminosity and of the number of visible interactions per bunch crossing denoted μ.

As the production of heavy quarks takes place predominantly at low angle with respect to the beam axis, the LHCb detector has been designed as a single arm forward spectrometer. High occupancy can degrade the tracking performance of forward detectors, thus LHCb was designed to work at a reduced luminosity compared to the general purpose detectors ATLAS and CMS. Hence, the instantaneous luminosity at the LHCb interaction point is reduced by increasing the distance between the two colliding beams in the plane perpendicular to the beam direction. While collisions and beam-losses decrease the beam intensity during an LHC fill, the transverse distance between the beams in LHCb is reduced, keeping the instantaneous luminosity stable within a $\pm 5\%$ range. This technique, known as luminosity levelling, minimises the effect of the luminosity decay, allowing the experiment to maintain the same trigger configuration during a fill and to reduce systematic uncertainties due to changes in the detector occupancy [2, 3].

Strong variations of luminosity, beam size, machine-induced background, ghost charge, satellite bunches and beam crossing angle are expected during the LHC operation in Run 3. Measuring the instantaneous luminosity in real time is essential for the operation of the LHC machine, in particular to guide the levelling procedure at the LHCb IP. A dedicated luminosity detector will be able to provide a real-time feedback to the LHC operators. During the LHC Run 1 and Run 2 operation, the activity in the LHCb calorimeter was used to infer the average μ at the LHCb IP. This information was based on the hardware-implemented L0 trigger, which will not exist anymore starting from Run 3.

A Radiation Monitoring System (RMS) [4], a set of Beam Loss Scintillators (BLS) [5] and a Beam Condition Monitor (BCM) [6] were used in Run 1 and Run 2 to monitor the beam-induced background. The RMS, based on the Metal Foil Detector (MFD) technology, was devoted to monitoring the radiation load on the LHCb inner silicon tracker sensors. It was composed of four stations hosting seven MFD foils each, read out at a maximum rate of 20 kHz. It has been dismounted at the end of Run 2 and will be reinstalled in Run 3, with upgraded readout electronics and foils.

The BLS was the only real-time system doing bunch-by-bunch measurements of beam background close to the LHCb IP. This system is made of two quartz radiators and four plastic scintillators, read out by photomultiplier tubes (PMT). The BLS is an inexpensive and reliable system read out independently of the LHCb DAQ system. It is always active and its output is fed back for the LHC operation in real time. However, its technology presents strong output non-linearity and important detector effects.

The BCM, designed for operation at the nominal LHCb Run 1 and Run 2 luminosity, is LHCb's main "life guard". It comprises two stations of eight diamond sensors each, placed 5 cm and 4 cm away from the beam axis, respectively. It can be read out at a maximum rate of $1/(40\,\mu\text{s})$. If the average energy deposit in three adjacent sensors is above threshold, the BCM triggers a beam dump. A BCM failure would cause a sizeable

LHCb downtime of at least a few days. This system is being consolidated for Run 3 with an upgraded readout system.

Owing to the planned LHC luminosity increase, the LHCb detector is being upgraded to be able to cope with the new beam conditions [7]. The upgraded detector will start taking data in 2022 and will operate at luminosity values five times those experienced during Run 1 and Run 2. The experiment will switch to a new triggering scheme based on Real Time Analysis (RTA), relying on the entirely software trigger with significantly more flexibility in terms of physics output. For such a scheme to work, it is mandatory to maintain stable running conditions of the experiment.

One important parameter determining the running conditions is the instantaneous luminosity at the LHCb IP. In order to maintain the instantaneous luminosity, averaged over beam crossings, constant during an LHC fill and to measure the instantaneous luminosity for individual bunch crossings, a dedicated new small detector system will be built. This will allow operating the LHCb detector in stable conditions while measuring the luminosity in real-time. It has been estimated that for the online operation, a resolution of about 5% is required on the particle multiplicity. This is even more crucial for the upgrade of LHCb fixed-target programme with the new SMOG2 system [8] installed upstream of the LHCb Vertex Locator (VELO). From Run 3 onward it will rely on external multiplicity measurements in order to separate signal pN or NN$'$ beam-gas collisions from background of parasitic proton or ion beam collisions. It will fit in the space available upstream of the VELO (Fig. 1).

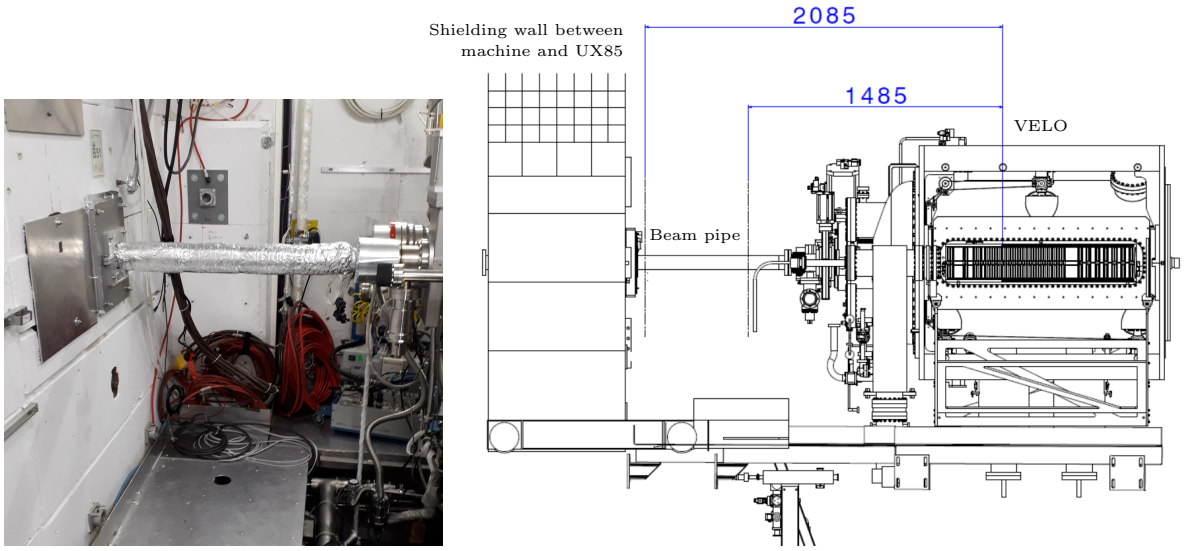

Figure 1: (Left) Picture and (right) drawing of the area upstream the LHCb Vertex Locator (VELO), which will host the detector measuring luminosity in Run 3.

During Run 3, the monitoring of the radiation level and of the beam-induced backgrounds will become even more crucial for maintaining reliable data quality and for extending the detector lifetime. Understanding of the background structure, the online monitoring and feeding back this information to the LHC are, therefore, essential features of the proposed new detector. Beam-induced background conditions will receive more careful monitoring at higher luminosity, with the goal of monitoring precisely the occurrence of bad quality vacuum and of undefined falling objects (UFOs) inside the beam

pipe. Unstable machine conditions as well as issues during beam injection, will trigger real-time response from both LHCb and the LHC itself.

The new detector should fulfill the following tasks:

- deliver the online luminosity and μ measurements for the luminosity levelling,
- perform these measurements per bunch,
- measure the radiation background induced by the accelerator or bad vacuum, produce alarms, measure the level of the ghost charges,
- cross-check the LHC filling scheme in real time,
- contribute to the centrality determination in the heavy-ion programme,
- provide accurate offline luminosity determination.

The readout system will be designed with a dual setup capable to deliver real-time data both in stand-alone mode and within the common LHCb DAQ system.

The accuracy of the luminosity measurement will be limited by the systematic effects. The statistical error can be estimated knowing the occupancy of the detector units and the LHC revolution frequency of 11 kHz. For example, if the average number of hits detected by a detector unit (a photomultiplier with a quartz tablet as described in Section 3.1) per bunch crossing is 1% (see Table 5 for details), this gives $0.01 \times 11\,\text{kHz} = 110\,\text{Hz}$ rate of events. Therefore, in 10 seconds one detector element should provide $1/\sqrt{1100} = 0.03$ statistical uncertainty per bunch crossing. After summing over N bunch crossings the accuracy should improve as $1/\sqrt{N}$, so e.g. for $N = 1000$ the same accuracy of 3% should be achievable in 0.01 seconds. This should be sufficient for online purposes. For example, the luminosity levelling requires a measurement frequency of $\sim 1\,\text{Hz}$.

The systematic uncertainty is difficult to estimate in advance. It will be determined by the stability of the detector and of the electronics and the quality of the calibration. The largest effect in the first category is expected to be the stability of the PMT gain values. The analogous system in ATLAS, the LUCID detector [9], has been operated in Run 1 and Run 2. It provided the best luminosity measurement for ATLAS with a long-term stability of about $\sim 1\%$. There are, however, important differences between the proposed LHCb system and LUCID. In particular, the proposed calibration method for LHCb is based on the monitoring of the peak from the primary tracks originating from the IP.[1] If the electronics of the proposed LHCb detector system will be operated in the threshold mode, it will be important to constantly monitor and to correct the threshold cut efficiency with the PMT gain varying with occupancy, time, and due to radiation-induced ageing.

This report describes a new, dedicated luminosity meter (luminometer) PLUME (Probe for LUminosity MEasurement), a small scale system that addresses the above requirements. It is based on photon detectors placed around the beam pipe and detecting

[1] In LUCID the best calibration is achieved using the signals induced by the integrated Bi–207 radioactive sources. A drop of Bi–207 was positioned at the surface of the PMT window, dried and then hermetically closed via a dedicated procedure before installing PMTs in the LUCID detector.

Cherenkov light emitted by particles traversing fused silica radiators, hereinafter referred to as quartz radiators. The GEANT4 simulation described in Section 7 demonstrates that such a detector could achieve its major objectives.

The Cherenkov light technology allows the signal to be produced and collected within a short time ($\sim 10\,\text{ps}$). A precise timing measurement most probably requires, however, the development of dedicated electronics. Therefore, the time determination at the sub-beam-crossing level is not discussed in this proposal.

The radiation resistance requirement for the system is the most critical aspect of this project, and the one which drives the design choices. Figure 2 shows a comprehensive view of the expected accumulated radiation dose during Run 3 corresponding to the integrated luminosity of $50\,\text{fb}^{-1}$, for the region between the shielding wall and the LHCb VELO [10].

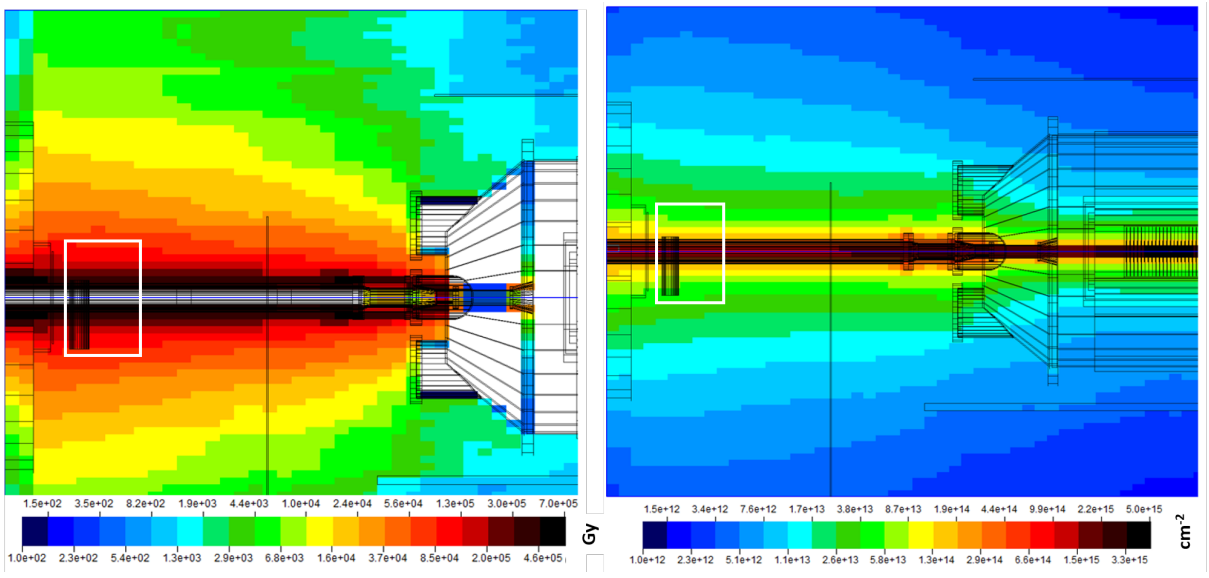

Figure 2: Total simulated dose accumulated during the LHC Run 3 corresponding to the integrated luminosity of $50\,\text{fb}^{-1}$ [10]. Displayed is the region upstream the LHCb VELO detector, view in the yz plane. The white rectangle indicates a location of the PLUME detector structure. (Left) Ionizing dose in Gy and (right) radiation dose expressed in 1 MeV neutron equivalents per cm^{-2}.

In the PLUME design, the photodetectors are operated with a small quartz tablet of 5 mm thickness to increase the light yield. The readout electronics is placed at the VELO platform and connected to the photodetectors with low attenuation 25 m long coaxial cables.

This Technical Design Report document is organised as follows. After this introduction, a short overview of the PLUME detector is presented in Section 2. The detector technology, the elementary detection module structure, the operation mode and the detector design are discussed in Section 3. Electronics and readout of PLUME are described in Section 4. Section 5 addresses the calibration and monitoring system. Infrastructure and cabling are discussed in Section 6. Section 7 is dedicated to simulation results, while luminosity determination is addressed in Section 8. Detector installation, operation and maintenance are discussed in Sections 9 and 10. Project planning, organization and cost are shown in Section 11. Section 12 summarizes the document.

2 PLUME overview

The new PLUME detector is outlined in this Technical Design Report. PLUME will play an important role in LHCb operation during Run 3. It will deliver online luminosity and μ measurements for the luminosity levelling; perform these measurements per bunch; measure the radiation background induced by the accelerator or poor quality vacuum, produce alarms, measure the level of the ghost charges; cross-check the LHC filling scheme in real time; contribute to the centrality determination in the fixed-target programme; provide accurate offline luminosity determination.

The detector is based on registering Cherenkov light produced in quartz material by particles coming from the collision region. An elementary detector is a photomultiplier with a quartz entrance window with an additional optically connected quartz tablet. An elementary detector has a small size with a typical expected occupancy of around 1% and a negligible probability to receive a contribution from two particles within one bunch crossing sampling. Therefore a yes/no counting will provide a reliable input to the logZero method of luminosity determination. Following the experience of ATLAS LUCID detector [9], an alternative charge integration measurement is also implemented. Two sets of elementary detectors form cross-like structures surrounding the beam pipe on the two planes of the hodoscope. The presented design is based on a number of studies, in particular on those outlined in Ref. [11]. The PLUME elementary detectors will be positioned upstream from the collision area, in the region between the VELO and BCM detectors, between 1680 mm and 1900 mm from the nominal interaction point. Radially, the detection modules will be placed between 157 to 276 mm from the beam pipe axis.

The PLUME information will be available both online, for fast online luminosity determination, and offline together with the rest of the LHCb data. Both functions are realized by the same readout system, connected to the LHCb ECS and DAQ systems. The electronics chain is based on reusing the components developed for the LHCb calorimeters.

Calibration and monitoring of PLUME rely on LED light delivered to the front side of each elementary detector via long quartz fibers and on the tracks reconstructed in VELO stations and traversing PLUME elementary detectors. The gain of photomultipliers, which can drift due to temperature, occupancy, extracted charge, radiation conditions and other factors, and hit efficiency will be monitored. The approach to monitoring largely inherits from the experience of LHCb calorimeters and ATLAS LUCID. Using in addition tracks reconstructed in upstream VELO stations and passing through PLUME detector further improves the reliability of calibration and monitoring system.

A small number of elementary detectors will be installed in July 2021 in order to gain experience with PLUME operation during a planned circulation of the LHC beams in September-October 2021. The remaining detector will be installed during the winter shutdown 2021-2022.

3 PLUME detector

The PLUME detector will be positioned upstream from the collision region. A set of elementary detectors form a two-plane hodoscope to select tracks coming from the collision region. The small size and consequently small occupancy values of an elementary detector legitimate a counting (yes or no) approach. The choice of technology for elementary detectors is motivated in this Section. The PLUME detector layout, design and integration aspects are also addressed.

3.1 Choice of detector technology

The choice of detector is based on a set of technological requirements and exploitation considerations. A fast signal is required to be well within the minimum distance of 25 ns between two sequential beam crossings in order to avoid spillover and to ensure an efficient readout (Section 4). The amount of signal from a traversing particle should be significant, so that a potential threshold drift does not affect the precision of the luminosity measurement (Section 8), and well above the instrumental noise.

The use of radiation-resistant materials is imposed by the harsh environment. A target occupancy per detector element of about 1% or more provides sufficient amount of data for accurate luminosity determination (Section 8). Another constraint comes from the possibility to calibrate the detector using the tracks reconstructed in the VELO upstream stations (Section 8.1). According to the VELO geometry and to the simulation, the preferred position of the elementary detectors is close to the beam pipe. The elementary detectors will detect particles coming from the interaction point at angles ranging approximately between 5° and 10° with respect to the beam axis. Therefore, radiation resistance is a crucial requirement as the dose values in the considered area range between 80 and 200 kGy and the neutron fluence is around 1×10^{14} neutrons/cm^2 as it is shown in Fig. 3. It represents the estimated 1 MeV neutron equivalent fluence and radiation dose at $z = -1670$ mm from the interaction point in the plane perpendicular to the beam direction. The red dots indicate the elementary detection modules positions. The shadow on the right part of the two plots is due to the presence of a valve, a massive cylindrical structure, that was in place when the dose simulation was performed, and should be disregarded.

Several technological approaches have been tested and described in Ref. [11]. These comprise a photomultiplier with the quartz window; a garnet scintillator coupled to the photomultiplier; a quartz fiber bundle acting as Cherenkov radiator and serving to transport the generated light to a remote photon detector; a garnet scintillator coupled to the quartz fiber bundle; a system of parabolic mirrors transporting the light produced in a Cherenkov radiator or in a scintillating crystal. A sufficient amount of the produced signal, fast signal generation, a radiation resistance, robustness, production feasibility and cost effectiveness have guided the final choice.

The PLUME elementary detector is based on a photon detector registering the Cherenkov light emitted by particles traversing fused silica radiators, hereinafter referred to as quartz radiators.

As the number of produced Cherenkov photons is limited, the use of SiPMs is disfavoured. Their performance for low light level detection under high radiation would be significantly altered or would require an expensive radiation-resistant cooling system in

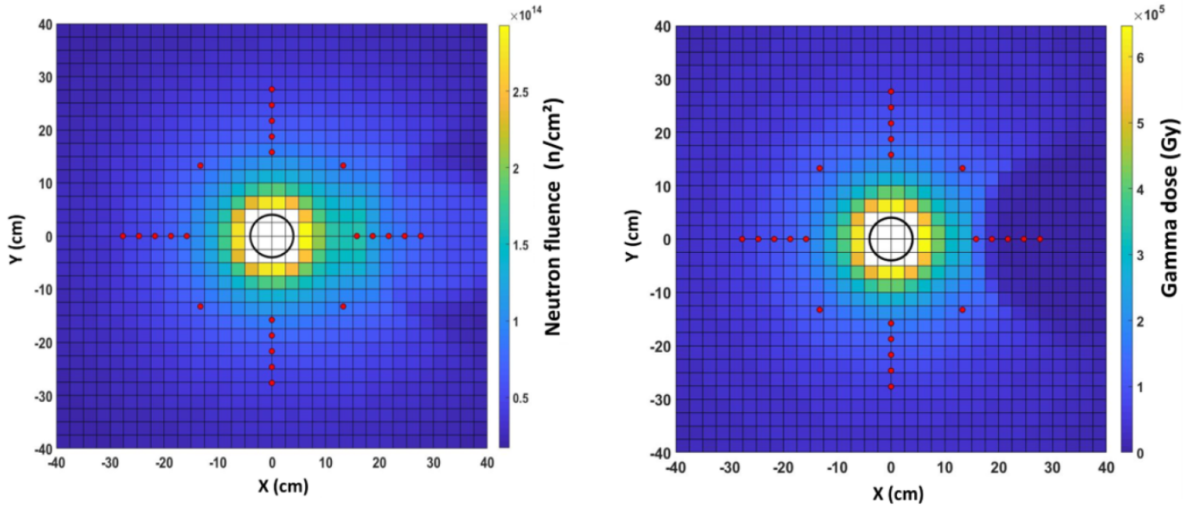

Figure 3: Estimated (left) 1 MeV neutron equivalent fluence per cm^2 and (right) radiation dose (Gy), corresponding to the integrated luminosity of $50\,\mathrm{fb}^{-1}$, at $z = -1670\,\mathrm{mm}$ from the interaction point, as a function of x and y coordinates, in the plane perpendicular to the beam direction. The values shown on the plots take into account a safety margin factor of 2. The red dots indicate positions of the elementary detection modules.

order to ensure their operation at temperatures down to -40°C. Therefore classical PMTs made with radiation hard materials like metal and quartz have been chosen for PLUME.

The R760 PMT produced by HAMAMATSU (Fig. 4) and successfully used in the LUCID detector [9, 12] is chosen for PLUME. The quartz window of this PMT is flat,

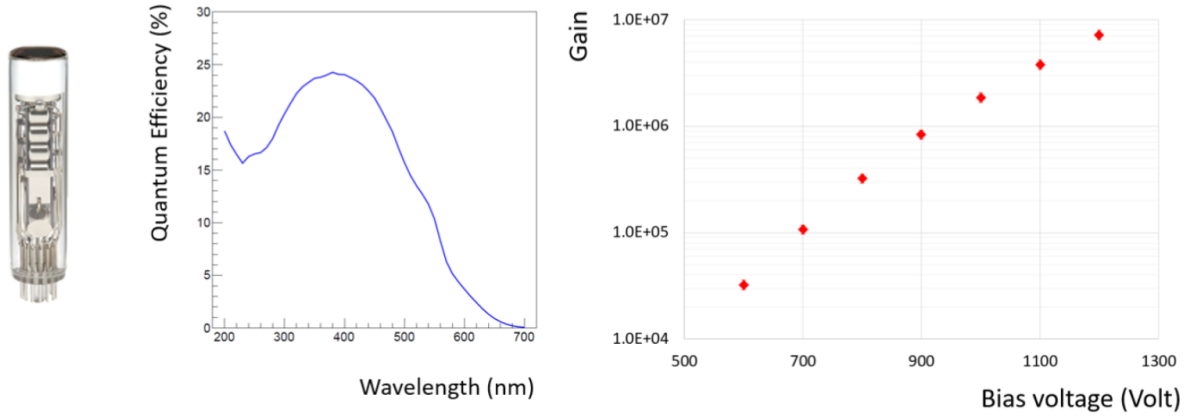

Figure 4: (Left) Picture of the HAMAMATSU R760, (middle) its quantum efficiency (in %) as a function of the wavelength (in nm), and (right) its gain as a function of the bias voltage (in V).

has a thickness of 1.2 mm and a photocathode with a diameter of 10 mm. Its quantum efficiency reaches its maximum for incoming light wavelength around 400 nm and exceeds 15% for wavelengths between 200 nm (about 6.7 photons produced per 10 nm spectrum bin in 1 mm thick pure fused silica) and 500 nm (about 1 photon per 10 nm bin per 1 mm thickness). The R760 had been tested under irradiation [13] with gamma rays up to $2{\times}10^5$ Gy dose and neutron fluences up to $2.7{\times}10^{14}$ neutrons/cm^2 and showed no variation of its spectral response and gain. The only observed effect to be taken into

account is an increase of about one order of magnitude of the PMT dark current that will lead to a dark noise frequency not exceeding 10 kHz. For the integration window of 25 ns, the charge corresponding to the dark current inside this window will represent 1/125 of the charge generated by a particle.

In order to increase the amount of produced Cherenkov light from the traversing particle, a 5 mm thick quartz tablet is positioned in front of the 1.2 mm thick quartz PMT window. This tablet has a round shape to match that of the PMT photocathode. A GEANT4 simulation was performed in order to estimate the gain in light yield due to the addition of the tablet. Figure 5 shows the GEANT4 model and the light yield distribution for the PMT window without and with the quartz tablet, assuming an ideal optical coupling (transmission factor of 100%) between the two quartz layers. According

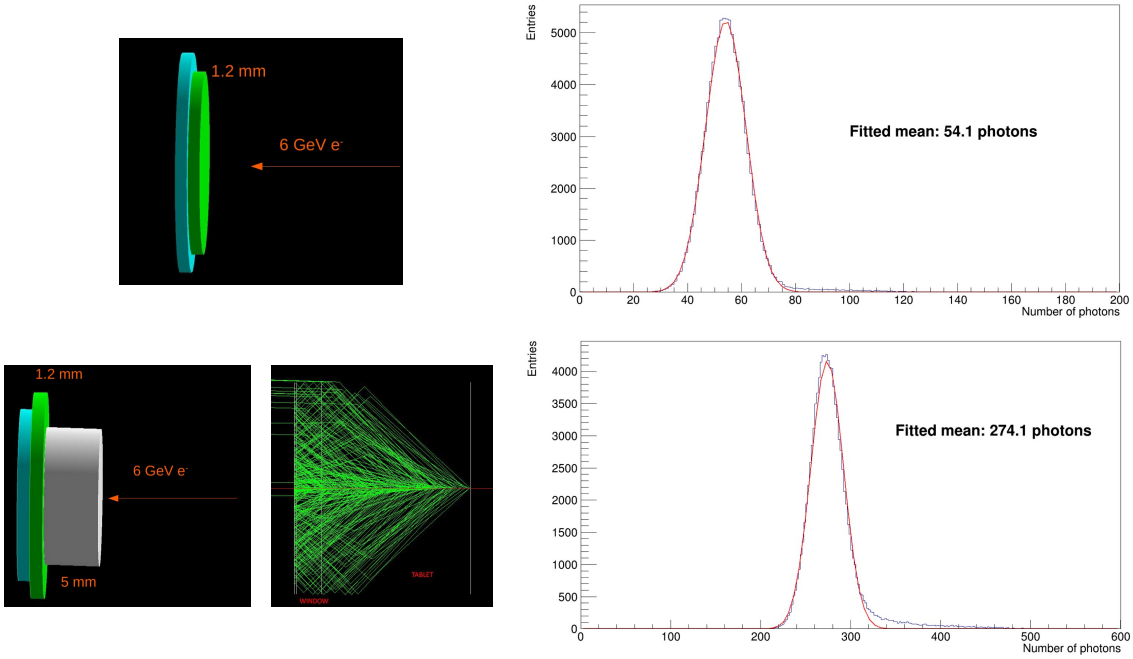

Figure 5: (Left) Simulated GEANT4 model for (top) the 1.2 mm thick PMT window and (bottom) the 5 mm thick quartz tablet coupled (transmission factor of 100%) to the same PMT window. For the latter case, the emitted Cherenkov photons are shown for illustration. (Right) Expected number of photons (300 – 650 nm) produced (top) inside the PMT window and (bottom) inside the quartz tablet coupled to the PMT window. The distributions are fitted with a Gaussian function.

to simulation, the addition of the quartz tablet increases the light yield by a factor 5. The quartz has to stay transparent to UV light under irradiation. The choice of the material is motivated in Section 3.3.2.

3.2 Elementary detection module

The elementary detection module layout is illustrated in Fig. 6. Each detector connected to its socket is fitted inside an Aluminium cylindrical shield that protrudes 20 mm beyond the window in order to also host the quartz tablet as well as a quartz fibre that brings the light to the front surface of the quartz tablet for the monitoring purposes. A permalloy

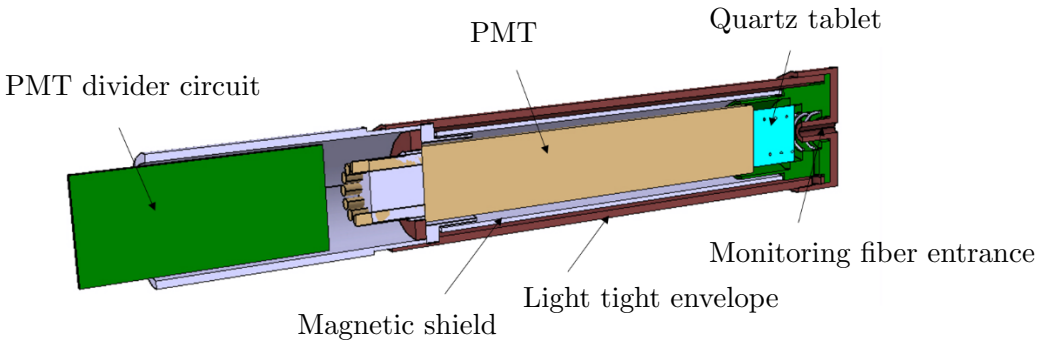

Figure 6: Schematic view of the PLUME elementary detection module. The module is 153 mm long with a diameter of 24 mm.

screen surrounds the PMT in order to eliminate a potential effect from the remaining magnetic field at the PLUME position. The screen extends the PMT by about 10 mm. In total, the elementary detection module is 153 mm long with a diameter of 24 mm. In order to lighten the structure, polyetheretherketone (PEEK) material will be used to encapsulate the module components. This material, compliant with the CERN Safety Instruction IS23 (Rev. 3) [14], is a semi-crystalline thermoplastic, which is resistant to radiation.

3.2.1 Photomultiplier R760

In order to determine the working point, the R760 photomultiplier was characterized. The experience of LUCID-2 was taken into account. LUCID-2 observed PMT ageing due to the drawn current with an accumulated charge value at the PMT output over Run 2 around 500 C [15]; the bias voltage had to be increased by 200 V in order to keep the gain constant. This continuous increase of the high voltage has a consequence on the PMT behaviour. It decreases the photoelectron transit time (Fig. 7) within the PMT leading

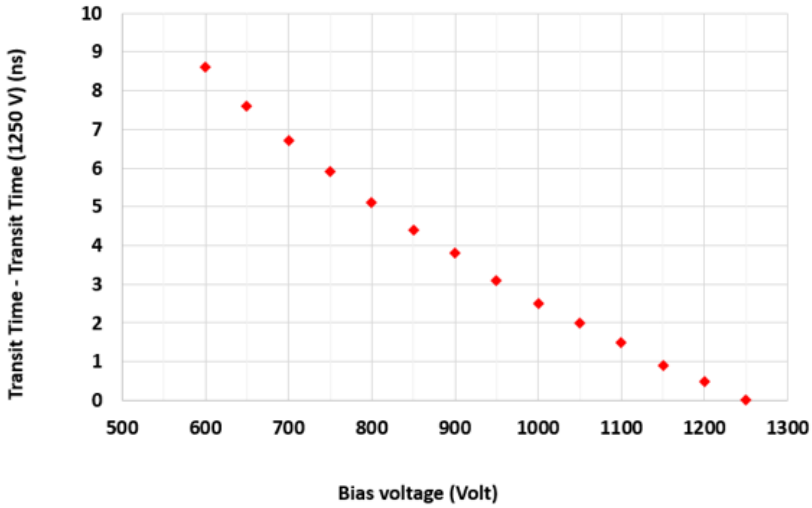

Figure 7: Transit time (ns) as a function of bias voltage (V) with respect to the transit time determined at 1250 V.

to changes in the signal timing. This effect has to be corrected for in order to guarantee good time alignment between LHC synchronization signal and PMT signal. Note that the R760 is biased with negative voltage and all the voltage values given in this text are absolute values.

Figure 8 shows the measurement performed with a pulsed laser (465 nm, 50 ps width FWHM) of the gain as a function of the bias voltage for an output charge of 3 pC and its deviation from linearity as a function of the output charge. The R760 PMT operated

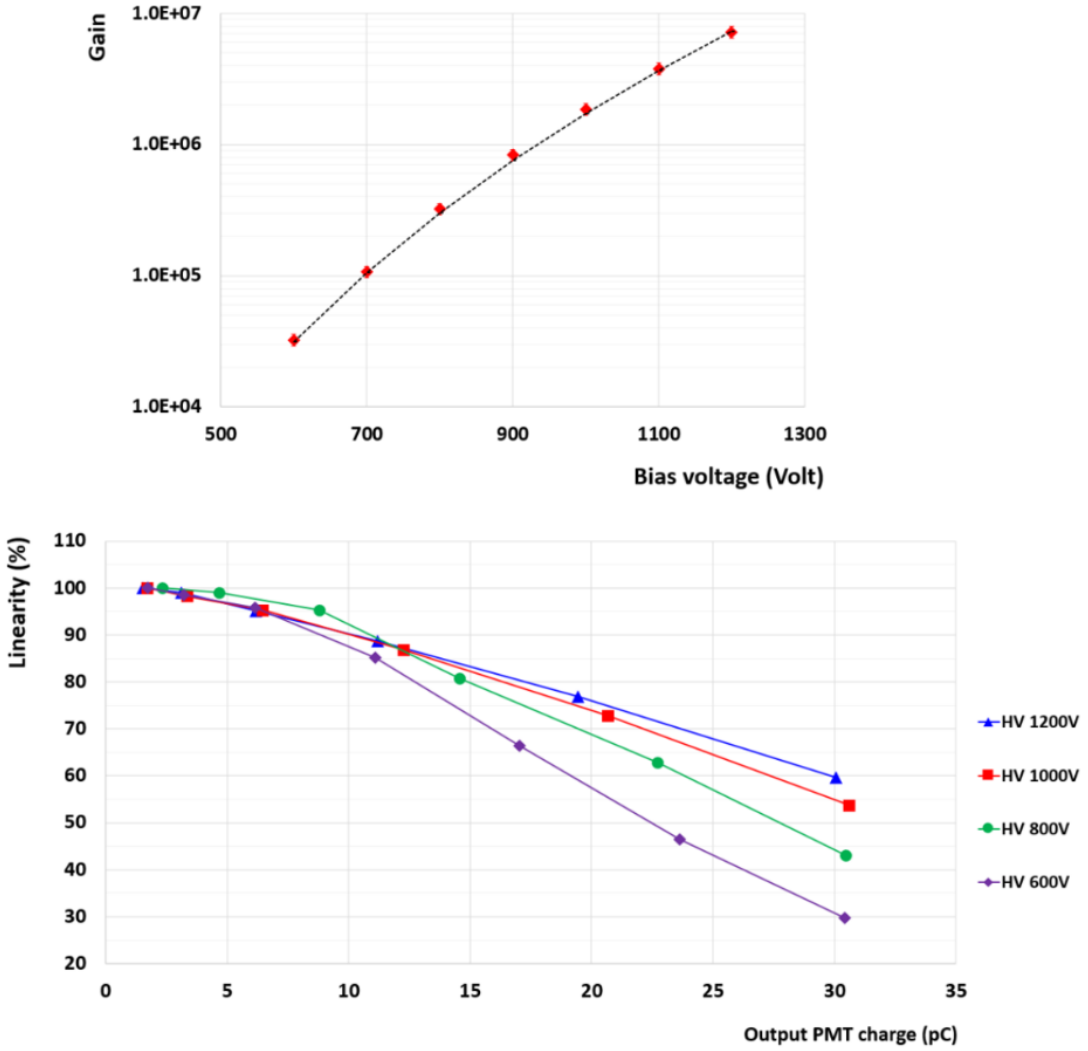

Figure 8: (Top) R760 gain as a function of the bias voltage (V) and (bottom) gain linearity (%) as a function of the output charge (pC) for four bias voltages (600, 800, 1000 and 12000 V).

with a standard resistive voltage divider is known to exhibit a limited linearity for short pulses, therefore all the gain measurements have to be performed with an incident light flux corresponding to an output charge smaller than 5 pC. We developed an enhanced resistive voltage divider which delivers a maximum current of 1 mA for a bias voltage of 1000 V. Its schematic view and the divider prototype are shown in Fig. 9.

This divider stabilized the gain of the PMT up to an average anode current of about 100 μA (Fig. 10) compared to the standard HAMAMATSU divider that can deliver an average current up to about 10 μA before non-linearity appears.

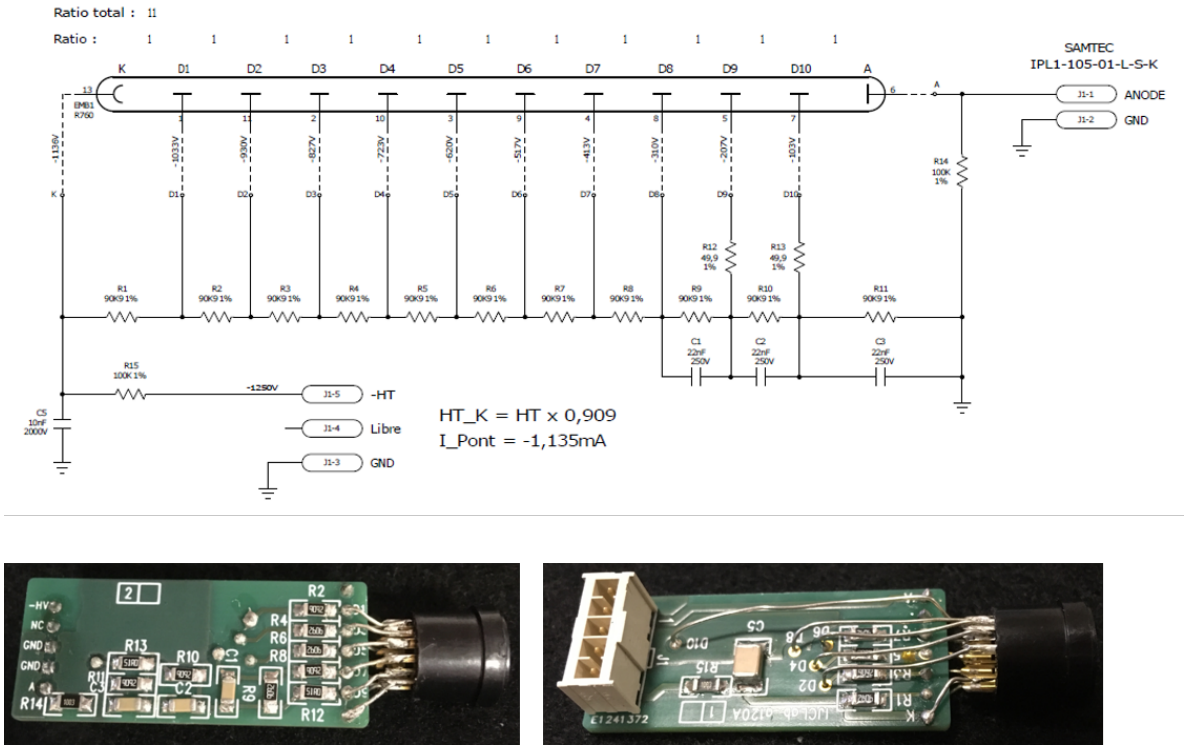

Figure 9: (Top) Divider circuit schematic view and (bottom) prototype divider circuit connected to the PMT socket.

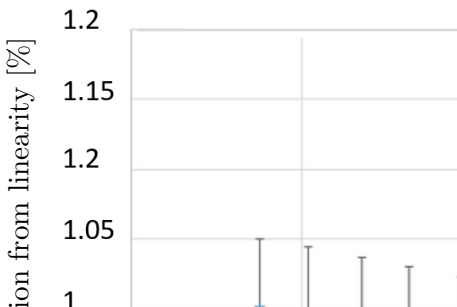

Figure 10: Deviation from linearity as a function of the anode current (nA) for a R760 with an enhanced divider circuit. The PMT was illuminated by an LED emitting light at 435 nm.

According to HAMAMATSU, the pulse current should not exceed 5 mA to guarantee a linearity better than a few percent. Taking into account this requirement, the pulsed linearity we measured that limits the output charge to 5 pC and the ageing effect for input signal corresponding to about 120 photoelectrons at the photocathode output, the gain of the PMTs should be set to 10^5, which corresponds to an average high voltage of approximately 700 V. The gain, dark current and quantum efficiency of each PMT will be measured before installation.

3.2.2 Quartz radiator

Transmittance of the quartz tablet has to match the Cherenkov light spectrum range and stand the expected level of radiation. Two quartz types have been considered: Corning HPFS 7980 and SPECTROSIL 2000. A good optical contact between the PMT window and the tablet will be insured using optical materials resistant to radiation [16–18].

A test beam was performed at DESY with 5.4 GeV electrons. Three configurations were investigated: PMT alone, where the Cherenkov light is produced inside the quartz window; PMT coupled to a polished quartz tablet of $10 \times 10\,\mathrm{mm}^2$ size and thickness of 5 mm, with TSF451-50M grease; and the PMT coupled to a frosted quartz tablet, where the light produced inside a polished quartz in direct contact with the PMT window would be reflected. The best result was obtained with the polished quartz tablet coupled to the PMT using the optical grease with a production of 125 photoelectrons per incident particle (Table 1).

Table 1: Charge collected at the R760 in different test configurations.

Tested detector	Charge (pC)
PMT alone	13
PMT + polished quartz	18
PMT + frosted tablet	22
PMT + polished tablet + grease TSF451-50M	37

Radiation resistance of the Corning HPFS 7980 quartz and several optical contact materials have been studied at NSC KIPT. The electron beam was sent to Tl target to deliver neutrons to the irradiated samples. As the Cherenkov radiation is more intense in the short wavelengths range (below 350 nm) and the fused silica transparency in UV suffers from radiation, the effect on radiator and grease transparency was studied at these wavelengths. Figure 11 shows the transmittance of 4 quartz plates measured at 200 and 250 nm before and after irradiation with a 1 MeV equivalent neutron fluence of 10^{14} neutrons/cm^2. A transmittance loss factor between 4 and 18% is observed.

Spectrosil 2000 (high OH and high H_2 content) used in the ATLAS Zero Degree Calorimeter under an irradiation rate of the order of magnitude of 100 MGy/year [19] exhibited a transmission loss around 20% on average and the transmission value is better than 40% for all individual wavelength in the 200 to 500 nm region. In order to validate the transmission loss caused by neutrons, an irradiation test with a fluence of $9{\times}10^{14}$ neutrons/cm^2 was performed at NSC KIPT in February 2021. After irradiation, a transmittance of 42% at 200 nm, 37% at 250 nm and 88% at 300 nm was measured.

Sandwiches of two quartz plates with optical contact material candidates (grease and glue) have been prepared at ISMA and irradiated at NSC KIPT. The results are

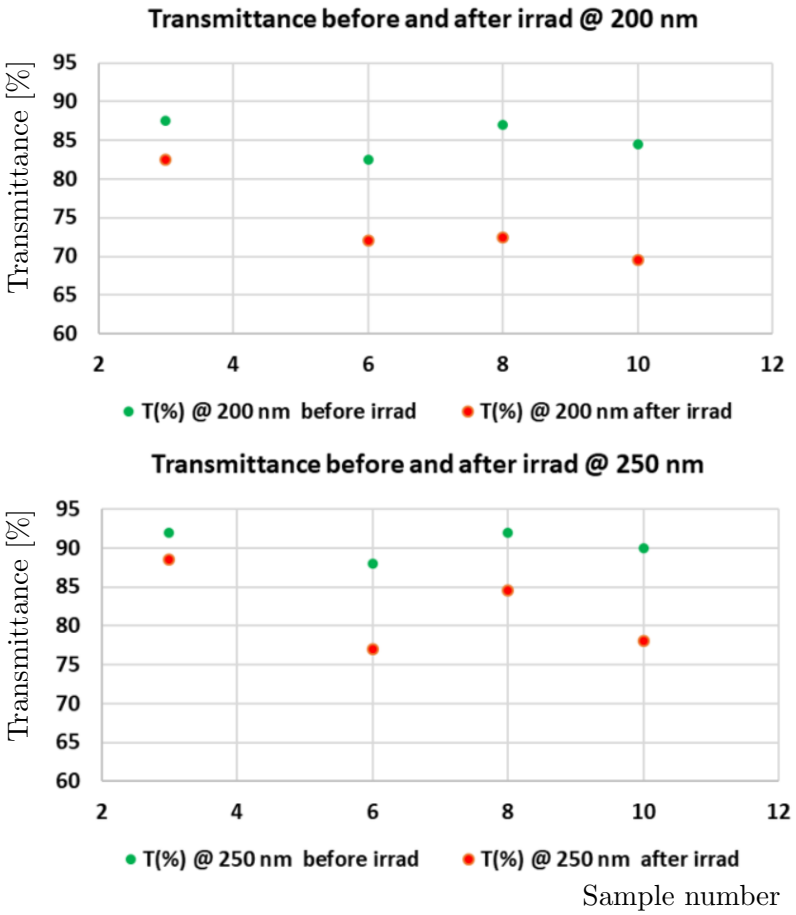

Figure 11: Transmittance (%) before (green dots) and after (red dots) irradiation of Corning HPFS 7980 quartz tablets at (top) 200 nm and (right) 250 nm. Only shown are the samples (numbers 3, 6, 8 and 10), which correspond to Corning HPFS 7980. Average over four samples is shown.

shown in Fig. 12 for two promising candidates, the Seiko-Silicone Grease TSF451-50M and SilGel-612. Black curves show the transmission before irradiation; red curves show the transmission after irradiation; and green curves show the transmission when the grease in the irradiated sandwiches is removed and replaced with fresh material. The difference between the corresponding green and red curves reflects the effect of radiation-induced degradation of the optical contacts. The Seiko-Silicone Grease TSF451-50M grease is chosen as the baseline candidate for PLUME detector.

3.3 PLUME detector layout

A total of 48 modules are arranged in a projective geometry and form a two-layer hodoscope. The first layer of PMT is positioned at 1680 mm from the nominal interaction point, the second at 1900 mm. The accuracy of the alignment in X and Y will be less than 1 mm. The alignment in Z is less constraining due to the significant extension of luminous region along the beam direction. In each layer, the elementary detectors form a cross around the beam pipe. The detectors are positioned at angles ranging between approximately 5° and 10° with respect to the beam axis. The exact detector angular positions are shown in

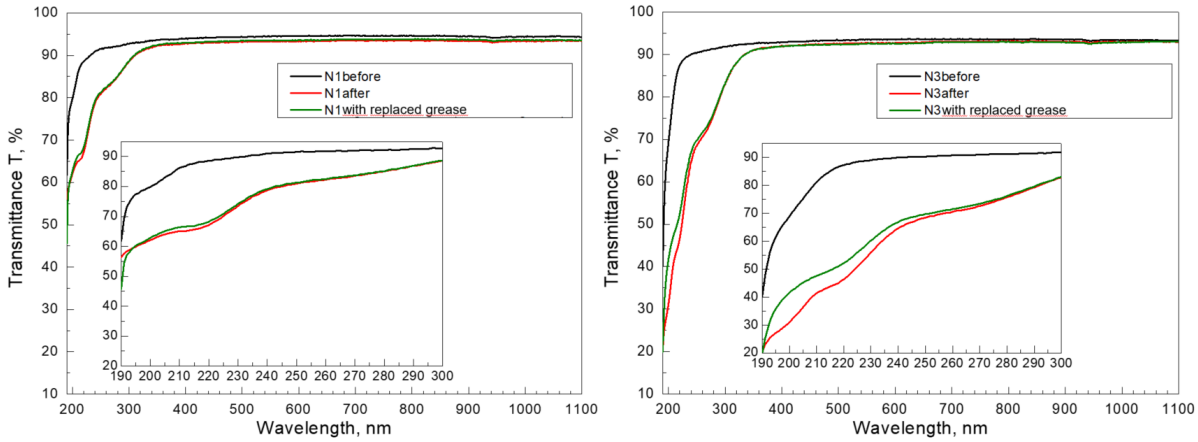

Figure 12: Irradiation of quartz sandwiches with (left) Seiko-Silicone grease TSF451-50M and (right) SilGel-612 grease as optical contacts. Black (red) curves show the transmission before (after) the irradiation; green curves show the transmission when the grease in the irradiated sandwiches is removed and replaced with the fresh material. Inserts zoom over the region 190 to 300 nm. Note that these tablets were made from the same type of quartz from, however, different production batches which explains a difference of their transparency.

Fig. 13. This corresponds to a pseudorapidity range $2.4 < \eta < 3.1$. The coincidence of

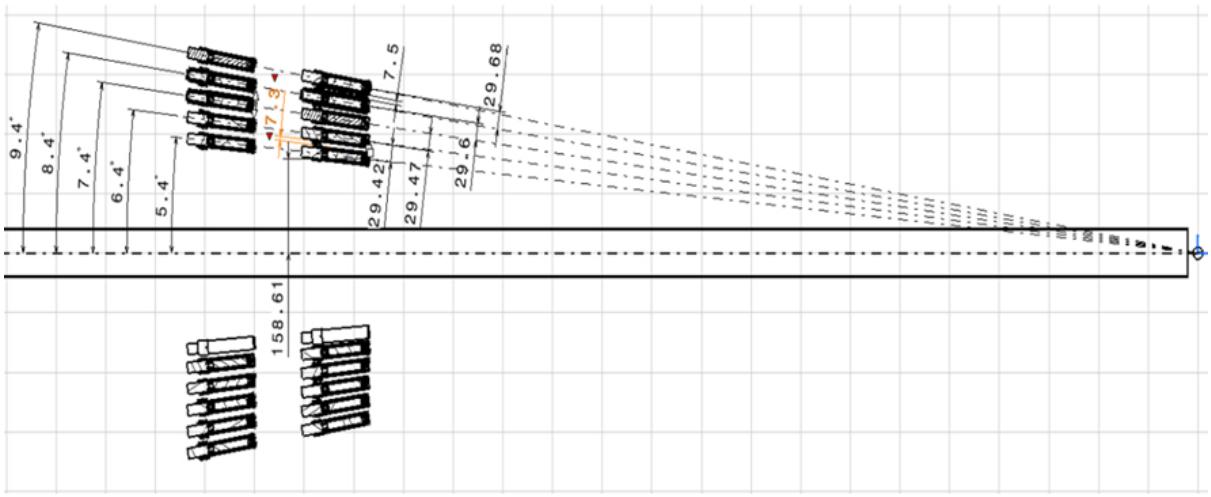

Figure 13: Angular positions of PLUME elementary detectors with respect to the nominal primary *pp* collision vertex.

two elementary detectors from the two hodoscope layers allows for cleaning of the sample of primary tracks for a standalone calibration. An even cleaner sample can be obtained using track segments reconstructed in the VELO upstream stations and passing through the hodoscope acceptance.

A cross of elementary detectors around the beam pipe allows the use of symmetry considerations. Deviations from this symmetry may provide information on the beam crossing angle.

3.4 Detector design and integration

The two cross-shaped aluminium structures, placed one behind the other, corresponding to two hodoscope planes, serve to support 24 modules each. The detector arrangement in the mechanical supporting structure is illustrated in Fig. 14 with side and beam views. An example of signal and bias cables connected to the rear side of one elementary detection module and the fiber connected at its front side is shown.

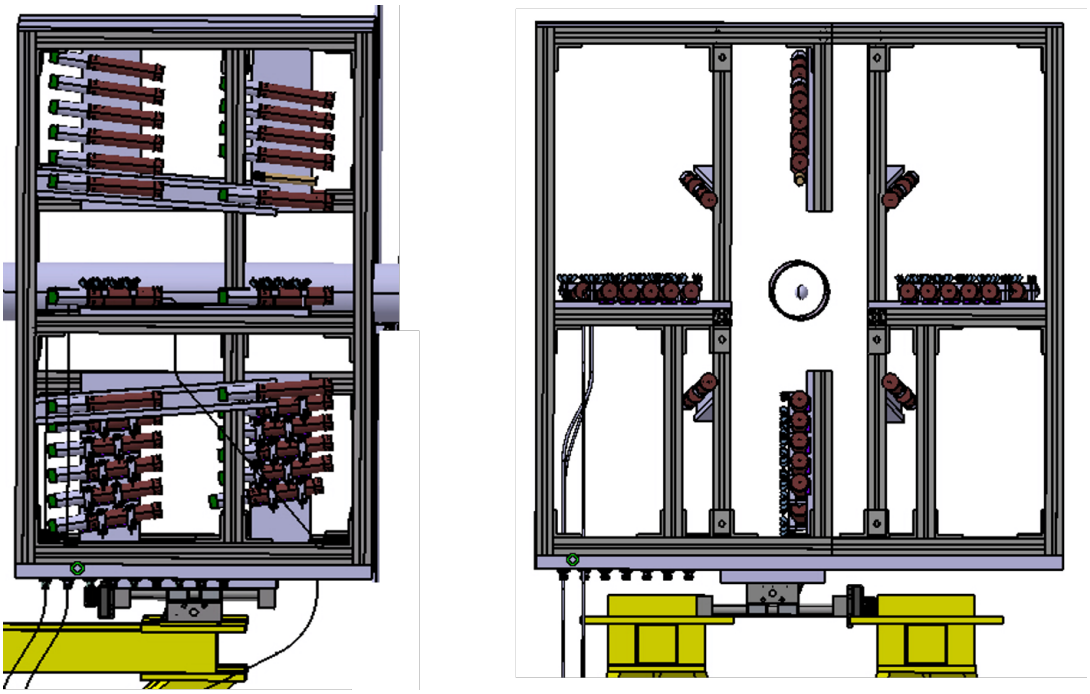

Figure 14: PLUME detector arrangement, (left) side and (right) beam views. Cable and fiber routing for one elementary detector module is shown.

The detector box is divided into A and C side parts and is mechanically protected from outside by a grid, which is common to VELO, SMOG2 and PLUME detectors. Grid elements can be removed to access the elementary detectors. A patch panel for cables and optical fibers is located below the detector. The PLUME detector box will be fixed to the wall by the means of two aluminium supports as shown in Fig. 15.

The integration of the PLUME detector in LHCb takes into account the neighbouring systems, in particular VELO, SMOG2 and BCM, and the infrastructure of these systems, the beam pipe and the vacuum system. In the downstream direction, compatibility with the VELO, the new SMOG2 system, and the eventual VELO maintenance procedure has been taken into account. Towards the IP, the envelope is restricted on side A by a cable of the residual gas analyzer (RGA) of the VELO vacuum system. In the upstream direction, a compatibility with the BCM detector system is required. A 128 mm clearance towards the RB84 wall is ensured in the PLUME design. Moreover, the BCM mechanical support will be redesigned with two frames allowing an extraction of the BCM modules to ensure the efficient access. The bakeout of the beam pipe is also taken into account.

The geometrical envelope of the PLUME detector ranges between $z = -1485\,\text{mm}$ and $z = -2085\,\text{mm}$ along the beam axis as shown in Figs. 16 and 17.

Other technical details are discussed in Ref. [20].

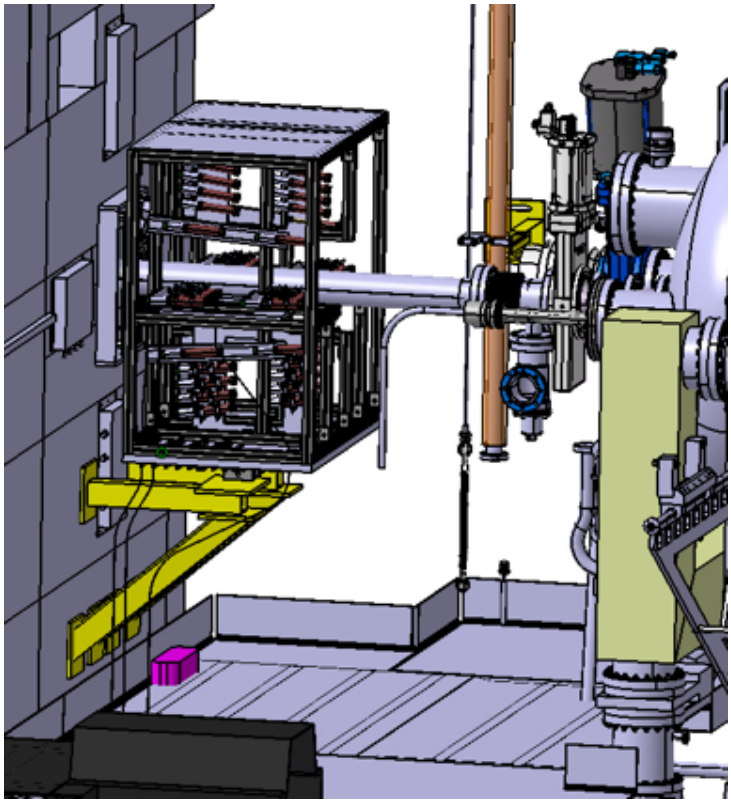

Figure 15: PLUME detector box fixed to the wall.

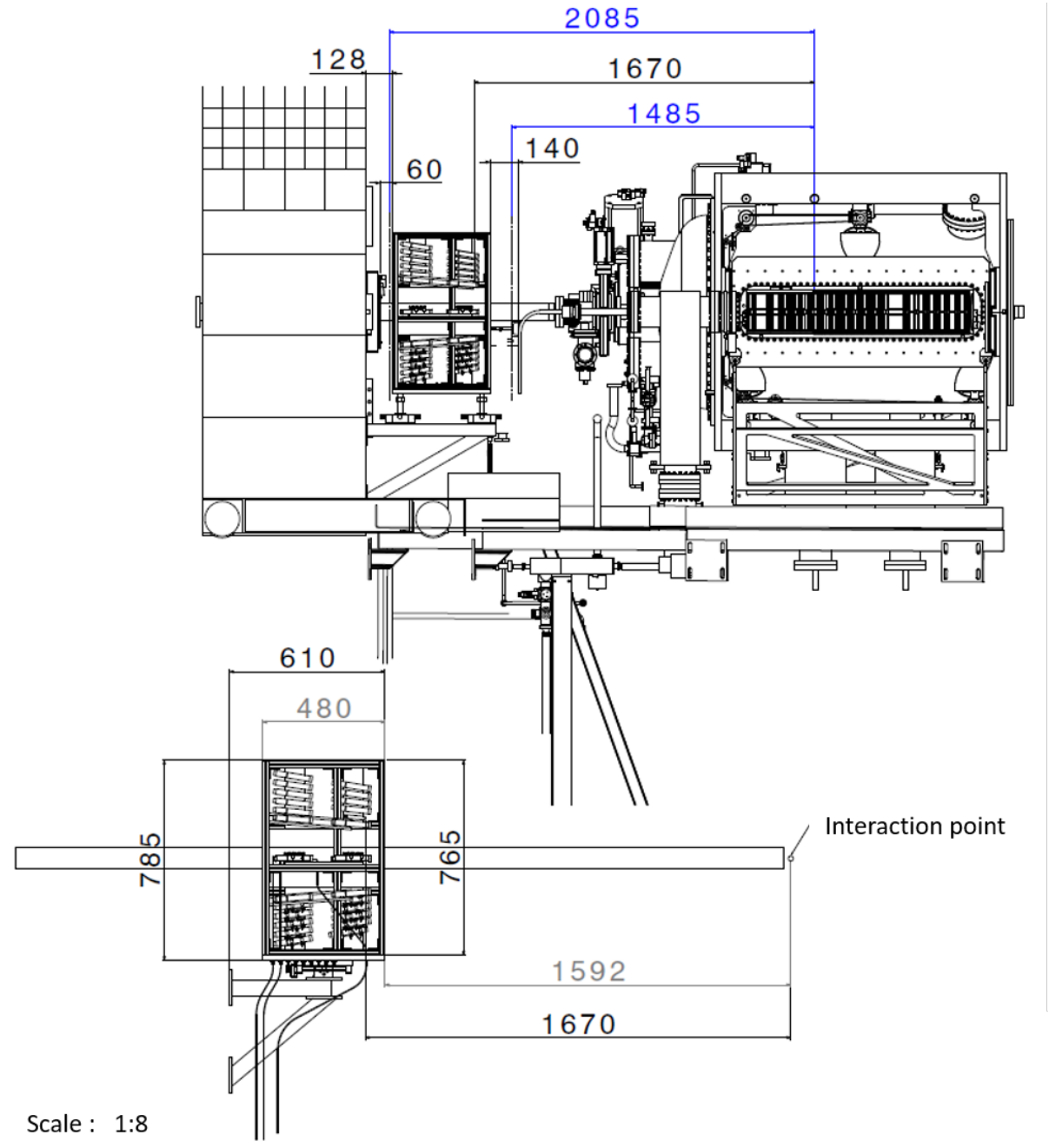

Figure 16: PLUME detector geometrical envelope. Side view.

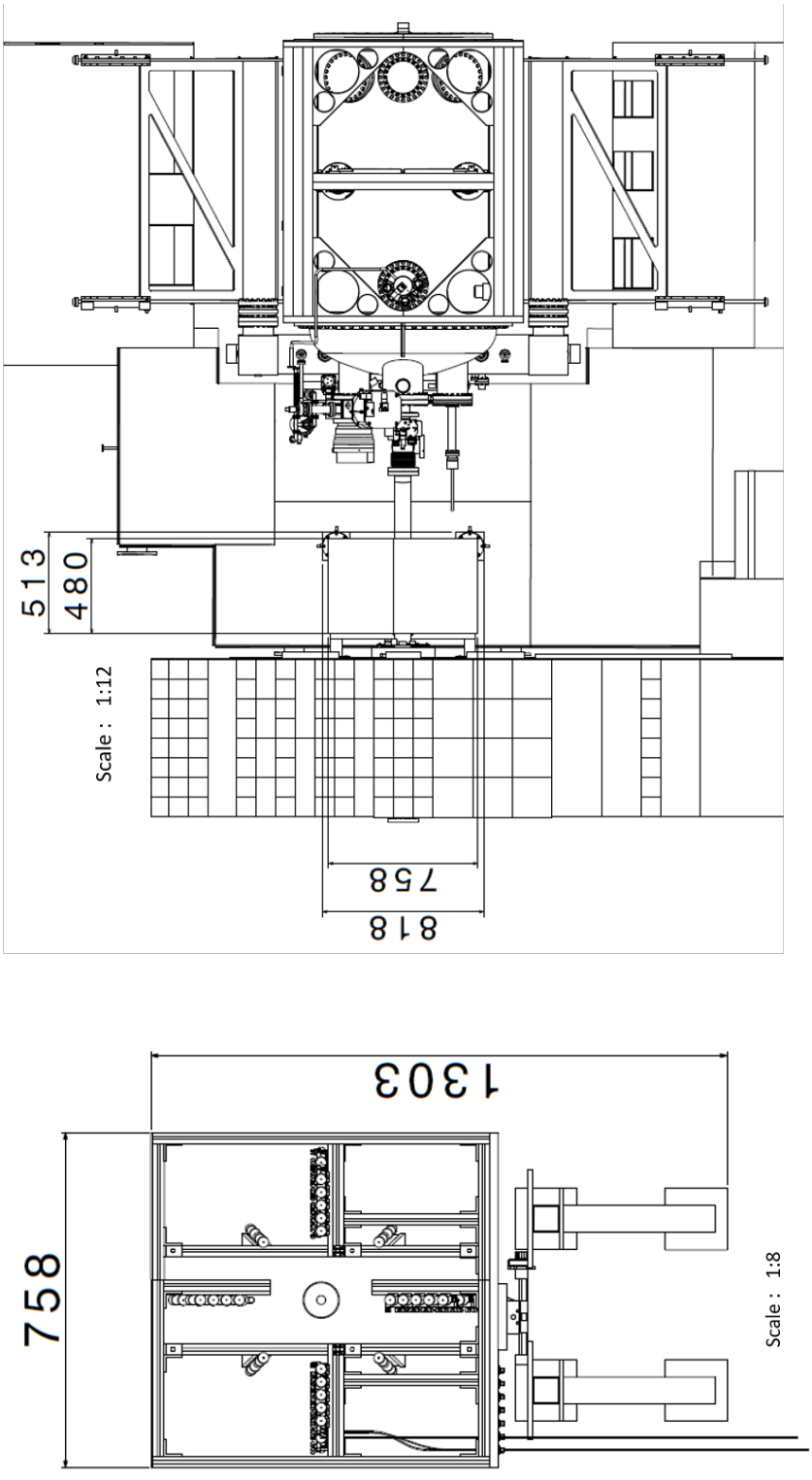

Figure 17: PLUME detector geometrical envelope. (Top) Top and (bottom) front views.

4 Electronics and readout

The PLUME information should be available both online, for fast online luminosity determination, and offline together with the rest of the LHCb data. Both functions are realized by the same readout system, connected to the LHCb Experiment Control (ECS) and Data Acquisition (DAQ) systems. The electronics chain largely reuses the components developed for the LHCb calorimeters and consists of a front-end (FE) part located close to the detector in the LHCb cavern and a back-end (BE) part. The PLUME readout elements are included in a dedicated partition inside the LHCb readout framework for ECS and DAQ. One particularity of the PLUME readout is that it should be running even if the other detectors in LHCb are not, in particular during the adjustment phase of the LHC cycle, when the value of the instantaneous luminosity at the LHCb IP is necessary for the LHC operator to prepare and optimize LHCb collisions.

4.1 Front-end electronics

The front-end components consist of 4 front-end boards (FEB) and 1 control unit board (3CU). They will be installed in a dedicated crate in the rack P1A04 on the balcony close to the VELO detector. Electronics boards are also needed for the PLUME calibration system and will be hosted in the same crate as the front-end electronics. These boards are described in detail in Section 5.2.

4.1.1 Front-end boards

Out of the four front-end boards, two are needed to readout the PLUME detector channels, one front-end board is dedicated to the monitoring system reading out the data from the PIN diodes, and another board is foreseen to perform precise timing measurement in the future. These front-end boards are the same as the boards designed for the calorimeter readout upgrade [21].

The role of the front-end boards is to amplify, shape and integrate the signal from the detector PMTs, using a custom chip, ICECAL, developed for the ECAL readout. The signal is then digitized by an ADC chip, and the digital output is processed in FPGAs. After formatting, the data are sent to the back-end electronics via optical fibers.

One front-end board can process a maximum of 32 channels. For each channel, the digitized ADC value of the signal is obtained with a dynamic range of 12 bits. In addition, a binary information indicates if the signal is above a threshold or not, in order to facilitate the processing of the data in the back-end electronics and in the software trigger. The value of the threshold can be programmed via the ECS in a register of the board, for every channel independently. The final data format transmitted between the front-end and the back-end electronics is coded on 112 bits per group of 8 channels as described in Table 2. Four fibers are connected to the front-end board to cover the 32 channels.

The calorimeter front-end board is reused without hardware modifications. Tests with realistic PMT signals showed that the analog part of the board is suitable for PLUME. Figure 18 shows the signal acquired by the front-end board for a pulse generated following the observed signal shape of a PMT used in the conditions of the PLUME detector.

The digital processing is performed on reprogrammable FPGAs. A large fraction of the data processing is identical in these FPGAs to the calorimeter processing. Modification of

Table 2: Data format of the PLUME front-end boards.

Bits	0...95	96...103	104...111
	ADC 12 bits per channel, 8 channels	Over threshold 1 bit per channel, 8 channels	Bunch crossing ID BCId

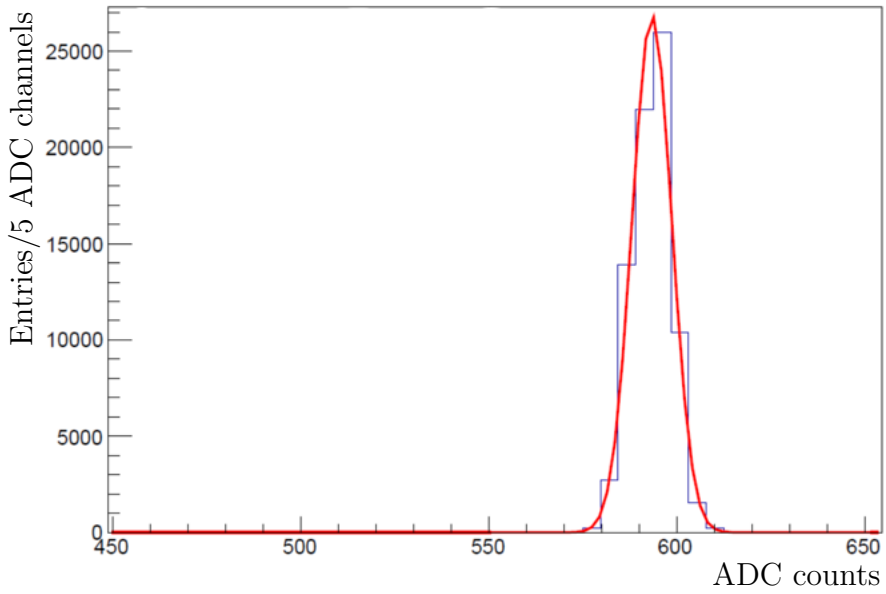

Figure 18: Pedestal-subtracted PLUME PMT signal after processing in the front-end board. The distribution is fitted with a Gaussian function.

the firmware is, however, necessary in order to provide the information whether a channel is over the threshold. The calorimeter front-end board also computes low level trigger (LLT) information which is not useful for the PLUME configuration. The corresponding firmware will be removed from the firmware developed for PLUME.

4.1.2 Control board

The control board (3CU) [22] transmits the clock, commands and configuration from the global LHCb systems to the front-end boards inside the same crate. For the PLUME setup, one 3CU board is needed. The same board as built for the calorimeter is used.

4.1.3 Crate

One crate with dedicated backplane is needed to operate the front-end electronics. The ones prepared for the calorimeter front-end electronics are used. It is a 9U crate with a water-cooled power supply. It is fed by a 380 V DC power line and controlled remotely with a dedicated control board. The control board and the 220 V AC to 380 V DC converter are placed in a radiation-protected area (B1 racks) and are connected to the front-end crate by long distance cables. This is identical to the low-voltage system throughout LHCb, and hence will be easily integrated.

4.2 Back-end electronics

The back-end electronics is implemented in the common LHCb readout board for the LHCb upgrade, the PCIe40 board [23], which is a PCIe based electronics boards hosting large FPGAs. The boards dedicated to data processing are called TELL40. One TELL40 board is enough to process the data from the PLUME front-end electronics. This board realizes two main functions: it computes the online instantaneous luminosity and formats the data sent to the high level trigger and to offline storage. These two functionalities are implemented in the firmware of the TELL40 board, inside the framework available within LHCb. One other PCIe40 board, dedicated to handling configuration, timing and control commands (called SOL40 board) is also required for the functioning of the system, with no specific modification needed for PLUME.

4.2.1 Online luminosity

The basic principle of the online luminosity determination (Section 8) is to count the number of bunch crossings without any visible interaction in the PLUME detector (logZero method). The fraction of this number compared to the total number of bunch crossings is linked directly to the luminosity. In order to reduce the effect of the noise, it is advantageous to combine the measurements from the two hodoscopes and to require time and space coincidence between the hits.

The firmware in the TELL40 will consist in producing a histogram with the number of hits in coincidence observed in PLUME. The fraction of events with no hits over the total of events is a measurement of the instantaneous luminosity as described in Section 8.2. Such histograms are also built as a function of the beam crossing identifier (BCId) in order to determine the luminosity per bunch crossing. The BCId is transmitted to the entire LHCb readout system from the readout supervisor [24].

The histograms filled in the firmware of the PCIe40 are read and cleared regularly, at a rate of about 1 Hz, by a script running in the ECS central system. The output of the script, *i.e.* the online luminosity, is transmitted to the LHC control system and archived in the central ECS database. The firmware and scripts are specific to PLUME and have no equivalent in the ECAL system. They are based on similar functionalities that were implemented in the ODIN readout supervisor during Runs 1 and 2 of LHCb. In order to monitor that the computations are done correctly inside the TELL40 firmware, the content of the histograms will also be sent to the online monitoring system where they can be compared with quantities obtained from the full PLUME data.

The computation of the online luminosity must be available even when the LHCb global DAQ is not recording data. This means the TELL40 board must be running constantly even when no data are sent to the event building network. In case of unavailability of the PLUME system, other systems in the LHCb detector are used as backup and temporary online luminosity providers, such as the beam monitor system.

4.2.2 Data formatting

The other function of the TELL40 board is to assemble the data received from the front-end electronics according to a well defined format. These formatted data will be sent to the high level trigger and be part of the global LHCb RAW event. The formatting firmware follows closely the calorimeter TELL40 firmware [25] since the input data are

almost identical to the calorimeter data, the only difference being that the calorimeter LLT information is replaced by the per-channel over-threshold information. The format is described in Table 3. In the default foreseen configuration, three front-end boards are

Table 3: Output data format of the PLUME TELL40 board (where the processing is done at 200 MHz frequency).

Clock period	Output frame (bits)							
	255...224	223...192	191...160	159...128	127...96	95...64	63...32	31...0
1	Thresholds FEB 0	Thresholds FEB 1	Thresholds FEB 2	channels FEB 0 ...				
2	... channels FEB 0							...
3	... channels FEB 1 ...							
4	... channels FEB 1			channels FEB 2 ...				
5	... channels FEB 2							Padding

included in the output data of the TELL40 board (two connected to the detector and one connected to the monitoring system).

4.3 DAQ

Software tools are developed to completely integrate the PLUME data in the global LHCb DAQ and Real Time Analysis (RTA) frameworks. The main item is the PLUME RAW event decoder, which will read the data out of the PCIe40 and transform them into objects usable by the LHCb analysis software, either in the high level trigger computations or for offline analysis.

In order to understand properly the PLUME detector properties, a simulation is provided. This simulation follows as closely as possible the real data flow and provides thus PLUME data with the same RAW data format as standard data. A software encoder ensures this feature in the simulation, emulating the PCIe40 data processing.

Finally, online monitoring is crucial to make sure that the PLUME data quality is optimal during the entire data taking. Monitoring algorithms will run in the online monitoring infrastructure and provide histograms and trend plots for the shift crew.

4.4 ECS

The PLUME detector is connected to the central ECS similarly to other LHCb detectors. The ECS components developed for PLUME cover the following functionalities:

- Configuration of the front-end electronics: front-end boards (including the one for monitoring), LED boards and the control unit;
- Configuration of the back-end electronics, the PCIe40 board;

- Control of the front-end crate: power on and off and monitoring of the consumption and temperatures in the crates;
- High and low voltages of the detector modules, including the setting of the high voltage with corrections computed by the monitoring system in order to compensate for ageing effects;
- Computation of the online luminosity, which is specific to PLUME, and transmission of the values to the LHC operators;

The PLUME control system is implemented in the global ECS of the LHCb experiment and complies with its requirements, implementing the proper finite state machine (FSM) elements and using the global ECS database to archive important quantities [26].

5 Calibration and monitoring

A crucial part of the PLUME detector is its calibration and monitoring system. The gain and efficiency of a PMT can change with time, depending on its current or detector occupancy, temperature and radiation dose. Two quantities will be monitored: the gain to ensure measurement linearity, and the hit efficiency for constant hit counting. The design for the monitoring system of PLUME follows the solutions implemented and tested in LUCID [9] and in the monitoring system of the LHCb calorimeters [27].

5.1 The monitoring system for PLUME

The monitoring system comprises two independent solutions: an LED calibration system and a calibration algorithm using upstream VELO tracks, i.e. those travelling away from the LHCb spectrometer. These approaches ensure the possibility to continuously monitor PMT stability, and to provide the precise calibration of the PLUME for the luminosity determination.

The PMT response to the LED light pulses delivered to the PLUME PMTs through the quartz fibres is monitored at regular time intervals using suitable gaps in the LHC filling scheme. The stability of the LED light pulses is in turn checked by PIN photodiodes placed next to the LEDs at the balcony where the radiation load is reduced. Finally, the degradation in the quartz fibres transparency due to the radiation damage is monitored with dedicated fibres looped back to the LED position and read out by the PMTs placed next to them. Based on the PMT response to the injected light, high voltage of the PMTs will be adjusted. Steps of $\Delta V = 0.5\,\mathrm{V}$ are available, corresponding approximately to a 2% gain variation. The LED calibration system controls are the same as those for the LHCb calorimeter monitoring system, and therefore are fully compatible with the LHCb detector.

An ability to calibrate PLUME response with VELO tracks dictates an overall PLUME geometry. The rapidity coverage of PLUME is chosen to overlap with that of the upstream VELO stations in LHCb, so that upstream VELO tracks are in the PLUME acceptance. For the calibration sample, events should satisfy the following criteria:

- have an associated track reconstructed in 4-5 upstream VELO stations and pointing to a given PMT;
- have a coinciding signal in the matching PMT of the second hodoscope plane.

The coincidence between matching PMTs of the hodoscope substantially suppresses secondaries. As discussed in Section 7, at $\mu = 8$ a coincidence between two PMTs is detected in 1.5% of the cases, with a primary to secondary particle ratio of $\approx 1:2$ to $1:1$ depending on the relative position of the two layers. According to the simulation, the coincidence between two PMTs is sufficient to get a clean signal of particles from the IP for PLUME calibration. An effective acceptance of VELO tracks that are useful for PLUME calibration is enlarged by reconstructing tracks both in the VELO closed and open position. In addition, a spread of the vertex positions across the collision region will produce tracks reliably reconstructed in VELO, which will cross PLUME hodoscope in a larger angular range. Corrections to account for the vertex position are discussed in Section 8.

5.2 Components of the LED calibration system

Eight LEDs are flashed producing short pulses (<15 ns FWHM) by eight driver boards, illuminating a bundle of eight quartz fibres each. These fibres deliver the light to the PLUME PMTs. In addition, one plastic fibre per LED sends the light to the corresponding PIN photodiode, to correct for possible LED instability. The PIN photodiode signal is extracted through an amplifier board. Both signals are read out using the front-end boards (see Section 4). All these components are placed on the balcony.

The full system comprises the following hardware components:

- an LED timing unit, the LEDTSB [28]. This is a 9U electronic board installed at the readout crate. This board is configured through DCS, communicating through a copper e-link;
- an E-Link Distribution Module (ELDM), identical to the ones used in the LHCb calorimeter monitoring system. The LEDTSB module is configured via a GBT e-link. The ELDM is an adapter module between an optical GBT duplex link and copper e-links, with the design based on the VLDB board [29];
- the "light box". It contains eight LEDs with their individual driver boards and eight PIN photodiodes with amplifiers. This box is installed standalone. It takes LVDS trigger pulses, and provides light flashes to the PMTs and amplified PIN photodiode pulses to the readout crate;
- quartz fibre bundles delivering light to the PLUME PMTs;
- four R760 PMTs for monitoring quartz fibre transparency;
- a dedicated FEB for reading out the eight PIN diodes and four fibre radiation monitoring PMTs.

For most of these components, already existing calorimeter spares are used. The quartz fibre bundles will be produced, as well as the mechanics of the "light box". A modular design is developed to house an individual LED driver, PIN diode and amplifier, and their connections. This simplifies installation and eventual replacement of the components.

5.2.1 LED choice

The LED driver uses the Cree LC503 (blue, wavelength 460 ± 25 nm). Its wavelength is chosen to match a transmission maximum typical for quartz fibres as they age under the influence of radiation. The LED light is not focused and exposes fibres without a large variation across the bundle. From ECAL experience, monitoring of humidity and ambient temperature is not crucial, as the temperature and humidity at the pit are controlled ($T = 20 \pm 1°$, humidity $\approx 50\%$) [30].

5.2.2 PIN photodiodes

PIN photodiodes Hamamatsu S1223-01 are used to monitor the LED stability. If the LED amplitude changes, this effect will be corrected according to the ratio between the PMT and the PIN photodiode readings. The LED light is delivered to the PIN diode

through a clear plastic fibre Eska CK–40, a 1 mm diameter PMMA fibre produced by the Mitsubishi Chemical Corporation. The PIN diode and its amplifier are displaced and individually shielded, minimizing electromagnetic pickup of the LED driver board by the PIN amplifier. The amplifier used for the PIN diode is read out with the same electronics as the rest of the PLUME detector. The LED driver and the PIN amplifier are shown in Fig. 19.

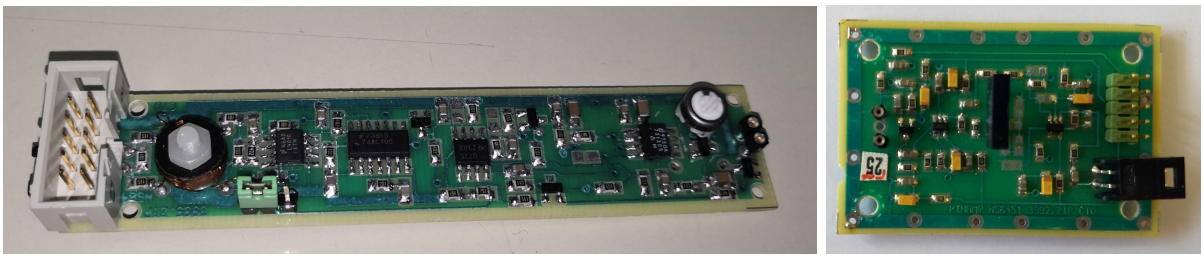

Figure 19: (Left) LHCb ECAL LED driver and (right) PIN amplifier, as used for PLUME.

5.2.3 Quartz fibres

Quartz fibres have been proven to tolerate radiation up to dose values equivalent to several years of exposure both at ATLAS [9] and at LHCb [27] (Fig. 20). In Ref. [27], fibres have

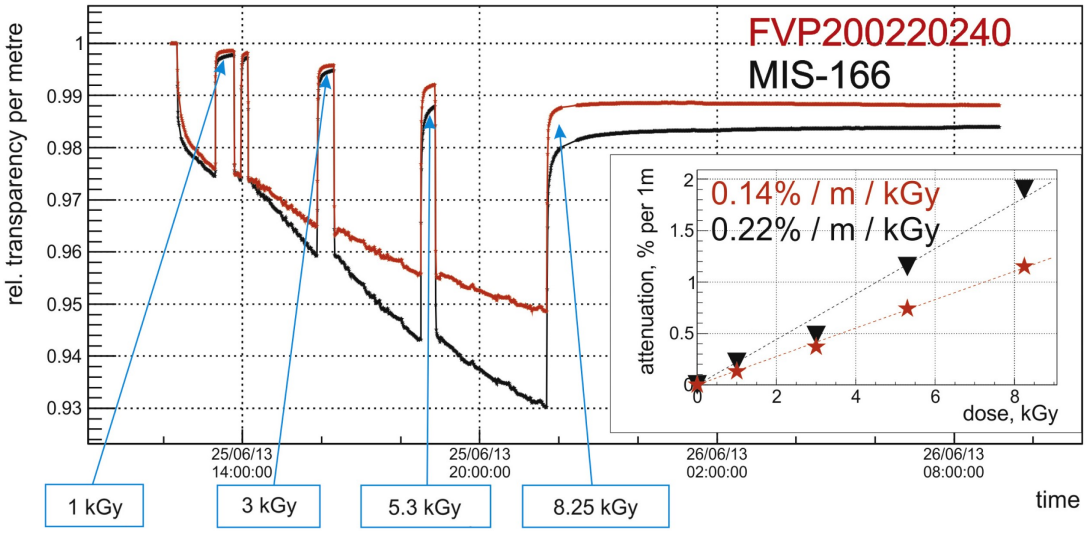

Figure 20: Relative transparency as measured during a quartz fibre irradiation test, showing the dose dependence of the stable damage part for two different fibres [27, 31].

been tested up to the radiation dose expected for the LHCb ECAL at the end of the LHC Run 4. A few % transparency degradation is observed during irradiation, but most of the transparency is recovered when irradiation is suspended. Persistent damage leading to the loss of $1-2\%$ transparency was reported at a dose of 8.25 kGy.

Close to the PLUME detector units, the fibres need to withstand a fluence of a few 10^{14} neutrons/cm^2 and a gamma dose of several 10^5 Gy (Section 3.1). However, only a relatively short length of the fibre is exposed to the harshest level of radiation,

and the remaining distance covered receives a much lower dose. Following investigations for CMS and the LHCb calorimeters [27, 32–36], it is estimated that over the total length of the fibre, an added attenuation from radiation of about 5.5 dB (72% loss) is expected. The dynamic range of the monitoring system is designed to be sufficient to balance this.

The fibres used in the LHCb ECAL monitoring system have a core diameter of 200 µm. With a higher gain in the PLUME PMTs (about 10^5, Section 3.2.1) than in the ECAL PMTs (2×10^3–2×10^4 [37]), a significantly lower amount of light is needed, and a diameter of 100 µm is chosen. Following ECAL experience [27], a set of fibres of type FBP (low-OH) and FVP (high-OH) was acquired from Polymicro and tested for its light throughput (Section 5.3). In the first quarter of 2021, these fibres have undergone an irradiation test to confirm that they can withstand the required level of radiation.

Five fibre samples (four from Polymicro [2], and one from OBS Fiber [3]) were irradiated using the LUE40 accelerator [38] with 80 MeV electrons on a tungsten target. The total integrated fluence on the target was about 1.2×10^{18} electrons. The fibres were irradiated by a mixture of beam-derived secondary electromagnetic particles and neutrons. At an estimated dose representative for PLUME of around 200 kGy and a neutron fluence of $1\text{-}2\times10^{14}$ n/cm^2, the irradiated section of the FBP100 fiber from Polymicro gave rise to a radiation induced attenuation of 0.50 ± 0.14 dB/m. No radiation induced effect has been observed for OBS fiber UVNSS90 product within measurement uncertainties. These results have been obtained 12 days after the irradiation and represent the long-term component of the radiation induced attenuation. Both these fibers are acceptable for use in PLUME, preference was given to Polymicro due to being an established supplier for the LHCb ECAL and other LHC projects.

Finally, quartz fibres are typically jacketed in a PVC or a similar halogenated plastic. For fire safety, these materials are to be minimized [39], and a PEEK jacket is foreseen.

5.2.4 Fibre bundle design

To account for quartz fibre degradation near the interaction point, an additional layer of monitoring is implemented. The fibre path is divided into three sections, interfacing through patch panels via SMA905 connectors. Short bundles splitting out into eight fibres are each illuminated by an LED. These couple to a long bundle (20-30 m) containing 64 fibres. At the second patch panel near the PLUME detector, 48 of these are coupled by short fibres to the individual PLUME PMTs. Another four short fibres (1-2 m) are used to loop the light back into the bundle, with those signals read out by four R760 PMTs placed on the balcony. These looping fibres are placed inside the PLUME frame such that they are representative for the short fibres going to each PMT. They are used to monitor additional fibre degradation due to radiation, in a way that is directly representative for all fibres in the bundle.

5.2.5 Power supplies

Four channels of high-voltage are extracted from the power cabling arriving to PLUME to provide the PMTs monitoring the quartz fibre bundle with power. Between the LED drivers and the PIN amplifier boards, a single channel each of +6V and -6V (PIN amplifier

[2] https://www.molex.com/molex/products/group/polymicro
[3] http://www.obs-fiber.fr/

power), +15V (LED driver power) and up to +30V (PIN diode bias) are needed. A further eight individually controllable low-voltage channels (up to +5V) will supply the control voltage to each of the individual LED driver boards, which determines the light output of the LED. A set of three Agilent N6700C mainframes with four remotely controllable power supply modules each are placed in the D3 barracks. The cables for transporting this power are described in Section 6. One mainframe and a set of four power modules is foreseen as spare parts.

5.3 A prototype for the PLUME monitoring system

A prototype of the holder for the plastic and quartz fibres is shown in Fig. 21. One

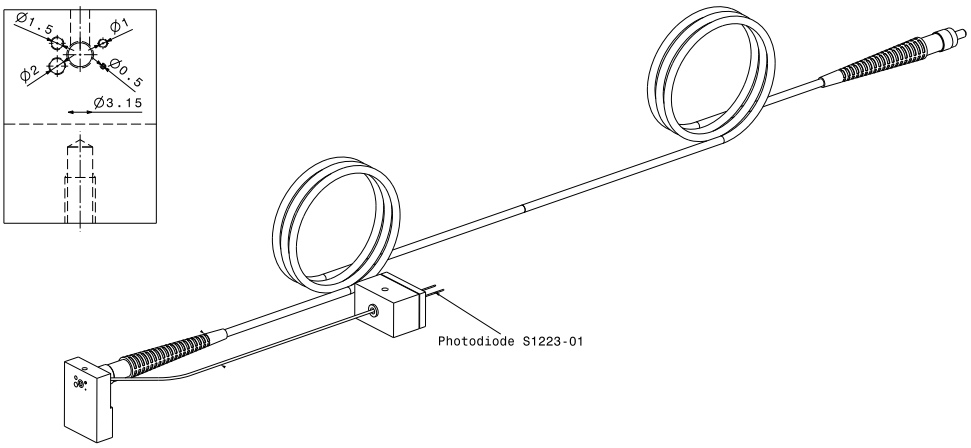

Figure 21: Prototype for fibre holder for light injection to PIN amplifier and into a quartz fibre.

quartz fibre and four Eska CK-style plastic fibres of different thickness are simultaneously illuminated with the LED. One plastic fibre is connected to the PIN diode and the quartz fibre to an R760 PMT. The electronics boards are shielded with 80 µm thick aluminium foil. The injected light is adjusted by neutral density filters and by the control voltage on the LED driver, staying in the linear regime of the HV divider. The time distribution of single photons arriving at the PMT is assessed by timing the leading edge of single photon pulses from LED. Neutral density filters were used to compensate the increased light yield as the control voltage was stepped up. This distribution represents the overall LED pulse (Fig. 22). The same setup measuring the LED light yield and the PMT gain, is also used to determine the light transmission for quartz fibres. The PMT light yield as a function of the PIN diode charge for five tested quartz fibres is shown in Fig. 23. Four of these were sourced from Polymicro, 50 and 100 µm core diameter, with high-OH content (FVP) and low-OH content (FBP). One was sourced from OBS fibre, 90 µm UVNSS. The light yield from the LED scales with the cross-section of the fibre. Fibres of type FBP100 coupled with the panel-mounting Thorlabs ADASMA connectors, as expected in the final design, were also tested.

The number of photo-electrons (p.e.) detected after transmission through a single fibre ranges from about 40 (200) p.e. at minimal control voltage to about 1.2×10^4 (5.3×10^4) p.e. at maximal control voltage, for 50 (100) µm diameter fibre, respectively. The thinner 50 µm fibre shows higher attenuation (about 0.6 dB) than the 100 µm fibre (below 0.3 dB), relative to the FBP100 fibre (#2). The attenuation added by a single Thorlabs ADASMA

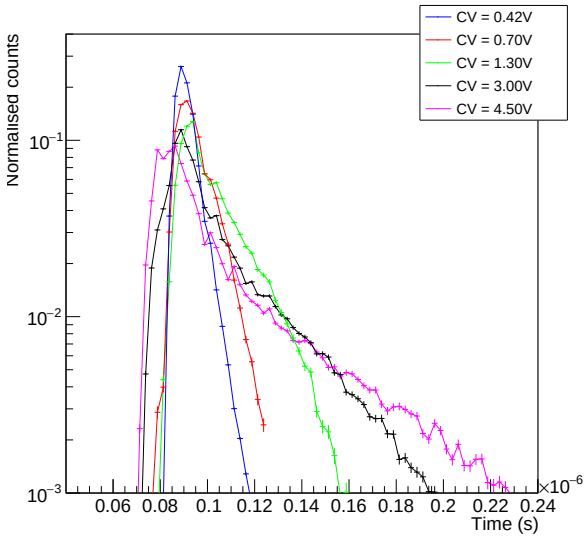

Figure 22: Time distribution of single photons sourced from the LED at various control voltages.

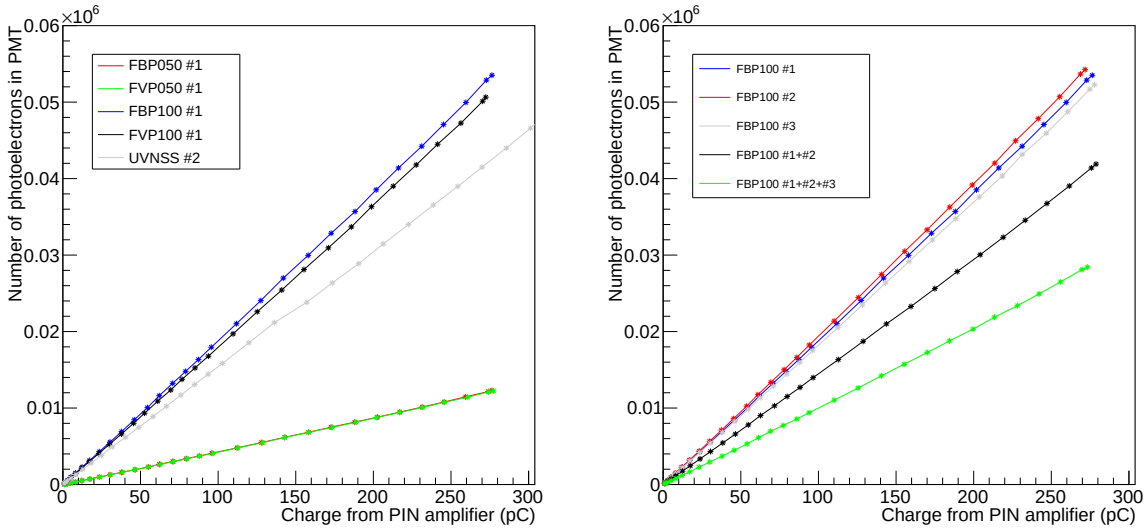

Figure 23: Number of photo-electrons observed in PMT EA2430 (left) for different fibre types and (right) for a set of FBP100 fibres, as a function of the charge in the PIN amplifier. For the black and green lines, a Thorlabs ADASMA connector was used to connect the fibres.

connector is about 1.1–1.2 dB. From the manufacturer's data, the absolute attenuation for the used fibres is about 0.04 dB/m, so the attenuation of a full-length PLUME fibre is about 3.7 dB, accounting for the length and two patch panels. Taking into account the added attenuation, the resulting light yield is close to that from a single MIP in the PMT front window, 25-30 p.e. The 100 µm quartz fibres allow to take into account the increased light yield from the MIP due to the quartz tablet (Section 3.2). Therefore, for the system with a quartz tablet, 100 µm fibres are chosen for the LED calibration system. The expected radiation losses are about 5.5 dB (72% loss). The dynamic range

of the LED driver is sufficient to deal with the expected added attenuation, including the double-length fibres to monitor radiation-induced fibre degradation.

The range of charge detected in the PIN diode is about 200-300 pC depending on the chosen settings (Section 5.4) for a 2 mm plastic fibre. Given that the front-end electronics (Section 4) have a sensitivity of about 11 fC/bin with 4096 bins (up to about 40 pC) the fibre of 1 mm thickness is used in the monitoring system design.

The PIN amplifier exhibits non-linear behaviour due to pulse clipping, a delay line with a deliberately unmatched resistor, optimized for an LHCb calorimeter signal shape. The cause of this is a change in signal timing as a function of the control voltage. An adjusted RC network will be implemented and cross-checked using VELO tracks.

5.4 Implementation of the monitoring system

The gain monitoring with LED light is organized as in the LHCb calorimeter system. Light injection is performed systematically at the beginning and at the end of each LHC fill, and at a rate of 50 Hz during data taking. The calibration tasks accumulate the amplitude measurements at light injection, saving and resetting the histograms every 15 minutes. The signals from the LED driver may affect more than a single 25 ns sampling, and are timed to match suitable gaps in the LHC filling scheme. If it is found that the gain change during the fill is not negligible, it will be controlled and corrected in parallel to accumulating physics data.

6 Infrastructure and cabling

The PLUME detector comprises four systems described before and schematically shown in Fig. 24: detector (Section 3), electronics and readout (Section 4), monitoring system

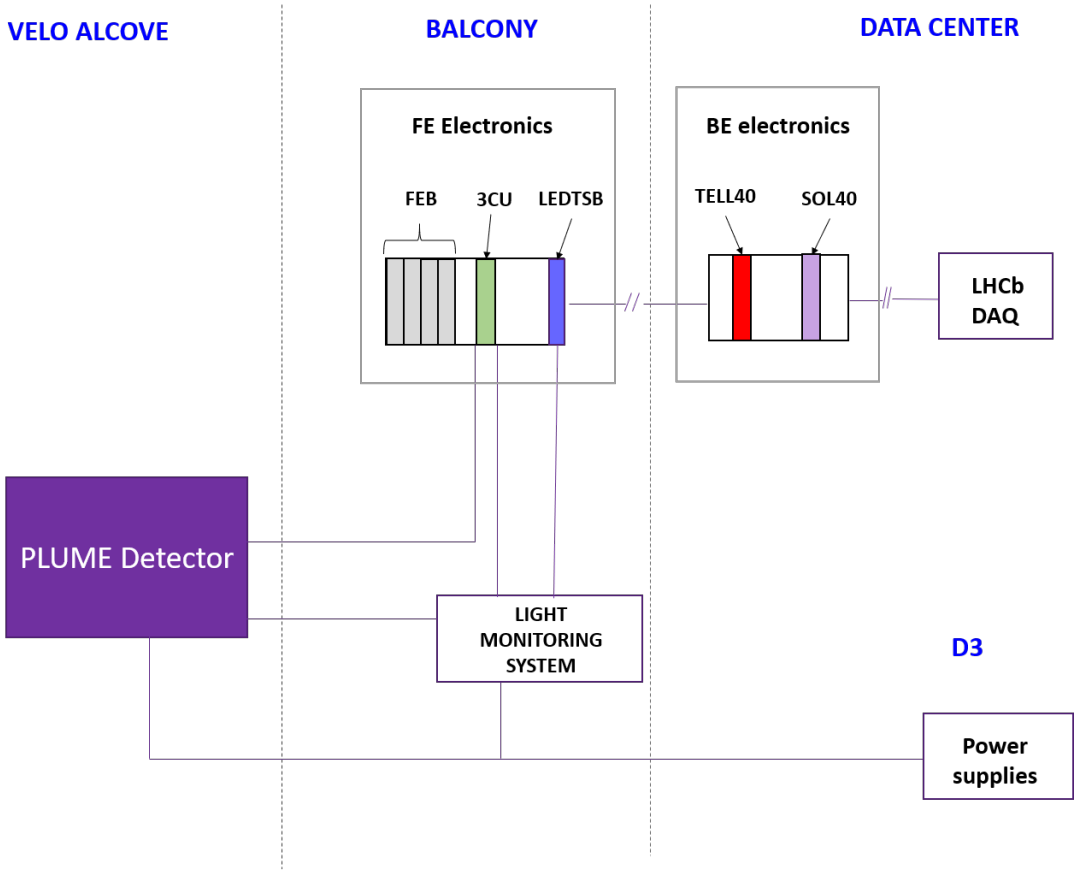

Figure 24: Schematic view of PLUME systems and their locations.

(Section 5), and services. Its components are located in the VELO alcove (detector), on the Balcony (FE electronics and monitoring system), in the data centre (back-end electronics and DAQ) and in the D3 barrack (power supplies).

The PLUME systems are linked via cables or optical fibers. The detector is connected to other systems via cables delivering high voltage to PMTs, cables reading out the signal and quartz fibers bringing monitoring light to each PMT. Figure 25 shows the schematic layout of the powering and cabling scheme. Table 4 decodes the notations used for the cables. All cables are compliant with CERN Safety Instruction IS23.

All cables and fibers will arrive from under the false floor below the PLUME detector box and will pass through the corresponding patch panels.

The PMTs will be biased via two high-voltage coaxial cables, each composed of 37 wires and connected to a CAEN multichannel power supply, consisting of SY4527 crate equipped with five AG538DN boards. This power supply is located in rack D3B06U. The transition between each 37-wires cable and the 48 individual cables that will bias the PLUME PMTs and the four ones needed for the PMTs of the monitoring system will be made by a distribution box located at the false floor level under PLUME.

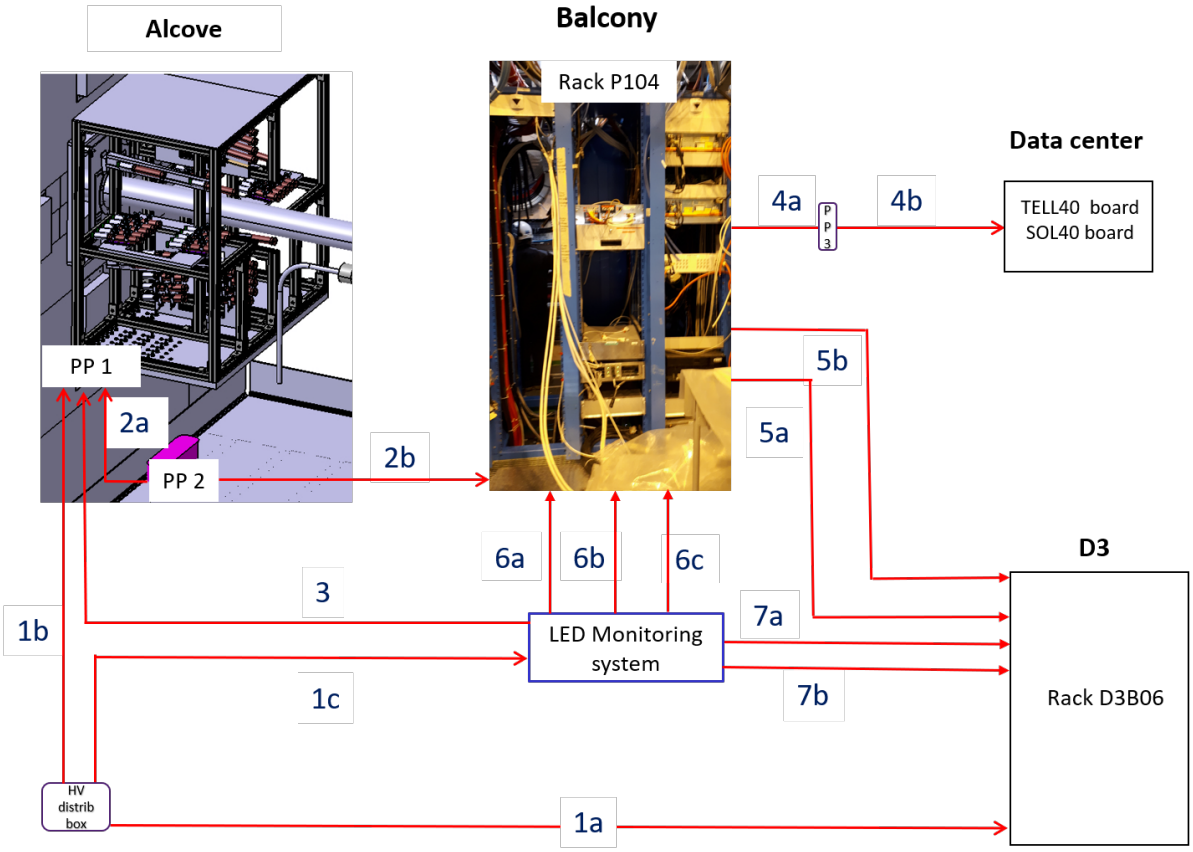

Figure 25: Schematic powering and cabling scheme. Cable codes are explained in Table 4

Table 4: List of cables for PLUME detector. Numbering of the cable types corresponds to Fig. 25.

Number	Type
1a	HV-37 wires
1b	HV (PLUME PMT bias)
1c	HV (Monitoring PMT bias)
2a	Signal (PLUME PMT)
2b	Signal (CK50)
3	Quartz fiber
4a	Signal DAQ+DCS
4b	Signal DAQ+DCS
5a	Power supply Rack P104
5b	CTL power supply Rack P104
6a	LED trigger signal
6b	Signal (monitoring PMT)
6c	Signal (monitoring PIN)
7a	Control voltages for LED drivers
7b	LED, PIN and amplifier bias

Signal coaxial cables connected to the PMTs dividers will pass through the PLUME patch panel (referred as PP1 in Fig. 25) and then through a second one (PP2) connected on its other side to 48 CK50 low attenuation cables that will bring the signal to the front-end electronics on the balcony. A bundle of 64 quartz fibres will distribute the light from LEDs over elementary detection modules for monitoring purposes. The number of the quartz fibers in the bundle includes both spares and eight fibers forming four loops at the detector side and dedicated to monitoring the effect of radiation on the optical fibers.

The routing of the cables close to the detector side is shown in Fig. 26. The magenta cable trays correspond to the new trays entirely dedicated to PLUME cables.

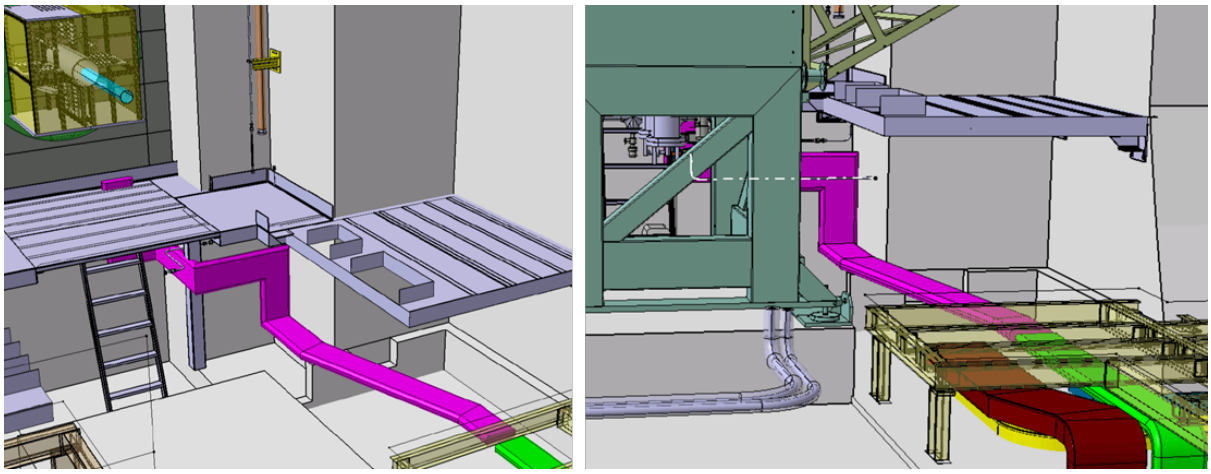

Figure 26: Schematic routing of the signal (CK50) and HV cables under the VELO (magenta and green cables trays). The magenta cable trays correspond to the new trays entirely dedicated to PLUME cables.

The PLUME FE electronics and monitoring system will be installed in the rack P1A04 on the balcony; to transmit the signal from the FE electronics (four FEB boards, one 3CU board) and the TELL40 and SOL40 boards, 16 fibers will be needed. The power supplies will be installed in the rack D3B06 in the D3 electronics hut. The composition of these racks is shown in Fig. 27. The cables and quartz fiber bundle connecting the detector and the P1A04 rack will arrive from the top part of the rack via existing cable trays. The CK50 signal cables with reduced mechanical flexibility will be guided along the sides of the rack until the PLUME FEE crate and will be connected to the front-end boards via a translation to the mini-lemo connector types installed at the boards.

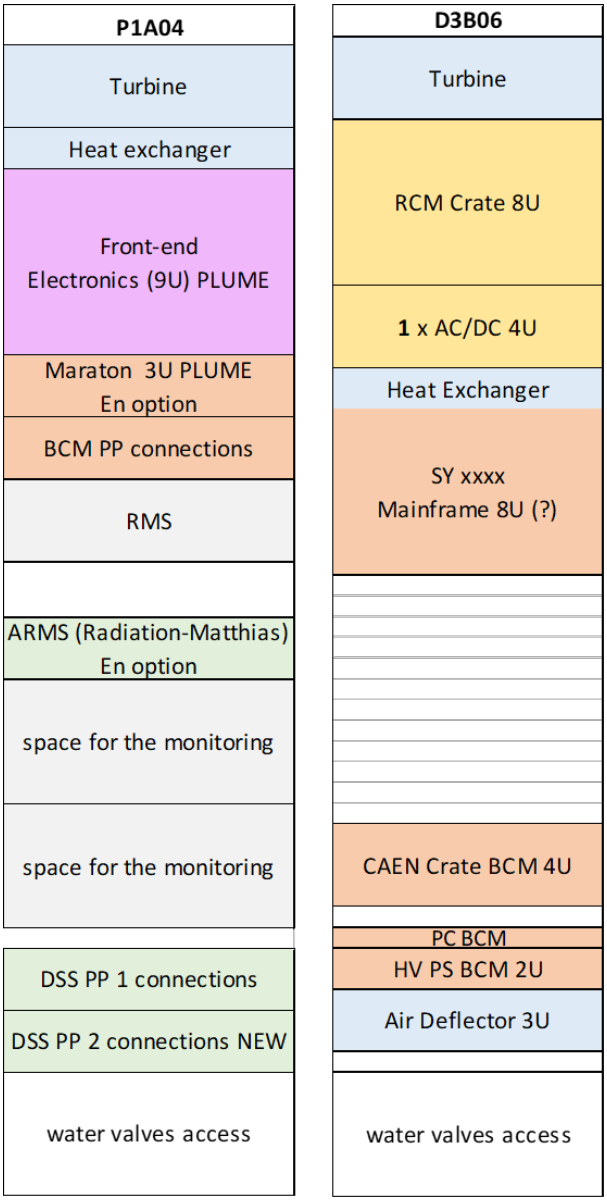

Figure 27: Rack layout.

7 Simulation and expected performance

In order to estimate the expected performance, a stand-alone Monte Carlo (MC) simulation is developed based on Pythia8 [40] (version 8.240) and Geant4 [41] (version 10.5.0) packages. The former produces particles in proton-proton collisions at a center-of-mass energy of 13 TeV, with a zero beam crossing angle, including both hard and soft QCD processes. Particles from the Pythia simulation, which will be called primaries in the following, are propagated to the Geant4 particle gun based on the default QGSP_BERT physics list with Cherenkov light radiation process and optical physics added.

The detector geometry implemented in the Geant4 simulation includes:

- VELO vacuum vessel as a stainless steel spherical cap with a thickness of 5 mm.
- Copper beam pipe with a diameter of 80 mm and a wall thickness of 1 mm.
- An equivalent material budget corresponding to the SMOG2 mechanical structure.
- Quartz material coupled to 100% efficient photodetectors.

Each photodetector is optically insulated by setting the light attenuation in the air to 10 μm. The simulation output is the number of photons collected by each detector per *pp*-interaction. Several Poisson-distributed interactions are randomly combined into "events" assuming the detector response is proportional to the number of particles. Empty "events" without interactions are also included in the sample and, by definition, contain no detected photons.

The diameter and thickness of the PMT quartz window are chosen to be 10 mm and 1.2 mm, respectively, as in the Hamamatsu R760 PMT. In a fraction of ATLAS LUCID detectors, half of the R760 window inner side was covered by a few nm opaque aluminium foil, thus improving the performance. According to the simulated results presented in the following, this will not be necessary at LHCb, where the occupancy is expected to be less but sufficient for 10 mm diameter PMTs.

According to the simulation, the distribution of the number of Cherenkov photons in the wavelength range of 300–650 nm, generated by a charged particle at a normal incidence in the 1.2 mm thick window, has a mean of 55 and a standard deviation of 11. On one hand, this light yield should be reduced by the R760 PMT efficiency shown in Fig. 4 middle. On the other hand, as it is also clear from this plot, R760 is sensitive to the wavelengths λ below 300 nm, where the amount of Cherenkov photons per unit length dx rises almost as $1/\lambda^2$ according to

$$\frac{d^2N}{dx\,d\lambda} = \frac{2\pi\alpha}{\lambda^2}\left(1 - \frac{1}{\beta^2 n^2(\lambda)}\right). \tag{1}$$

Here, $n(\lambda)$ is the quartz refractive index. The contribution of not simulated photons with the wavelengths below 300 nm significantly increases the light yield. In the end, the expected detected number of photons per track is around 30 according to LUCID [9]. The threshold applied in the present simulation is 65% of the signal for one track.

The simulated detectors are placed in the form of a hodoscope formed by PMT pairs with a projective placement with respect to the IP. The PMT themselves also point to the IP. Three z-positions at 6° angle with respect to the beam have been simulated as

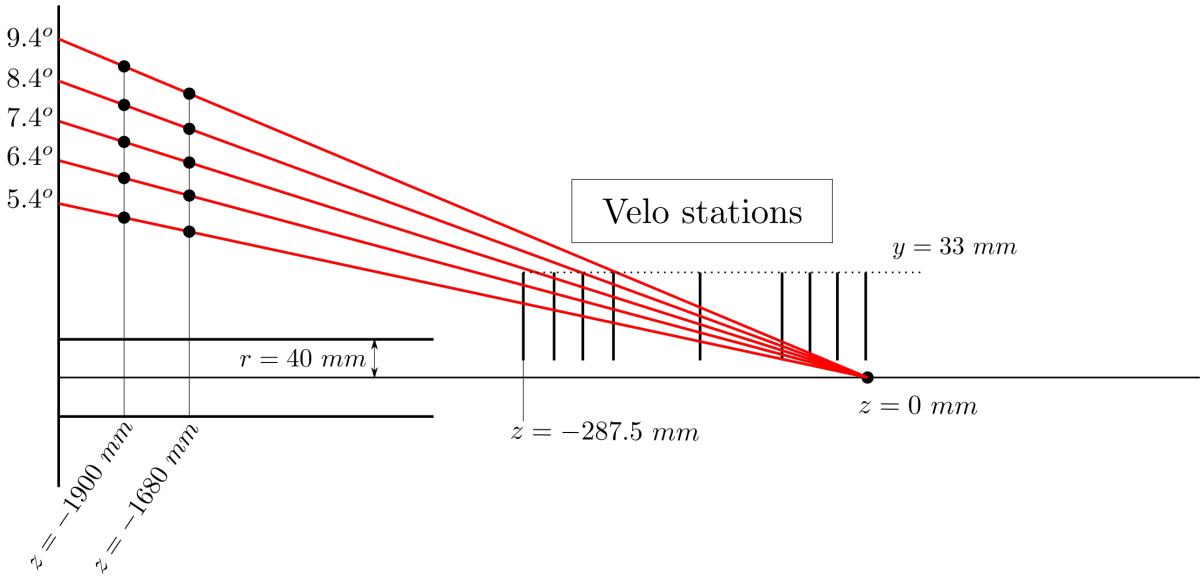

Figure 28: Schematic view of the simulated positions for two projective layers of PLUME elementary detectors. The first and second layers of elementary detectors are located at $z = -1680$ and -1900 mm, respectively. The corresponding angles with respect to the beam axis range from 5.4^o to 9.4^o. Positions of VELO stations are also shown. The red lines illustrate which VELO stations are expected to reconstruct a track firing a projective pair of PLUME elementary detectors. The plot is not to scale.

illustrated in Fig. 28. At this angle, a track coming from the nominal collision point (0,0,0) traverses five upstream VELO planes.

The simulated occupancy exhibits a small variation against z position of a detector layer. Table 5 shows occupancy at $\mu = 8$ for three z values obtained from simulation.

Table 5: Simulated probability to detect the number of photons exceeding 65% of the average one-track signal in the PMT without a quartz tablet for three simulated z-positions at 6° angle with the beam in an event with $\mu = 8$ Poisson-distributed interactions.

z-position, mm	Layer occupancy
-2070	4.2%
-1670	4.3%
-1270	4.7%

For the PMT layers situated at $z = -1680$ and -1900 mm, the occupancy of the first PMT layer and coincidence probability of projective PMTs are shown for five radial PMT positions in Fig. 29. One can see that all values are in the comfortable range $0.4 - 5\%$. With the LHC revolution frequency 11.245 kHz, even the lowest value 0.4% will allow to reach in one minute a statistical precision of the luminosity measurement per bunch of $1/\sqrt{4 \cdot 11.245 \cdot 60} \approx 2\%$.

A potential uncertainty caused by the description of particle multiplicity by the Pythia generator has been studied in detail in Ref. [42]. A large variety of Pythia versions are compared with alternative generators (Herwig++ [44], PHOJET [45]). The authors quote the largest difference of 37% between the simulation and the data.

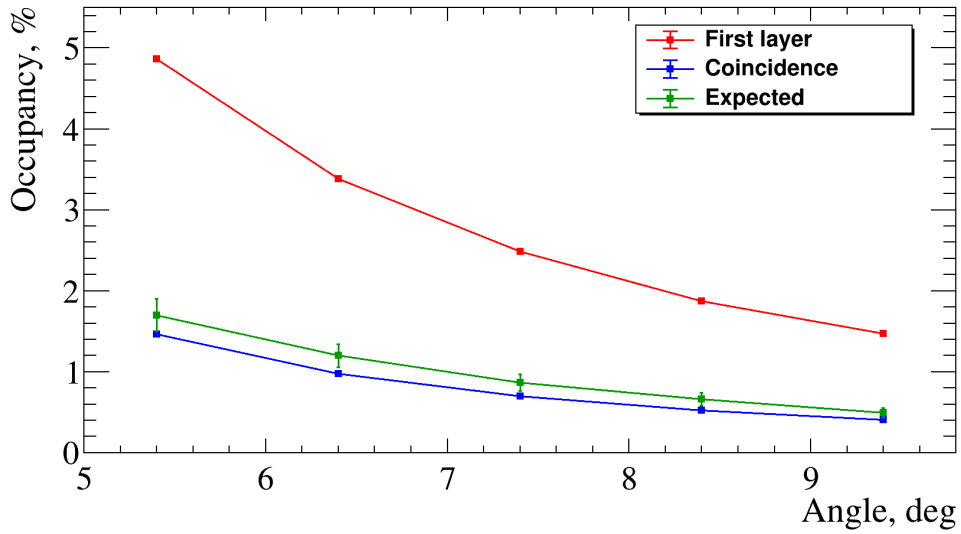

Figure 29: First layer occupancy (red squares) and coincidence probability between pairs of projective PMTs (blue squares) for $\mu = 8$ versus the angle with respect to the beam axis, in degrees. Green squares represent expected occupancy from charged tracks originating from luminous region projected from data using Refs. [42, 43]. The PMT layers are situated at $z = -1680$ and $z = -1900\,\text{mm}$.

Expected occupancy caused by tracks coming from primary pp collisions can alternatively be evaluated using the measurement of charged particles multiplicity in the forward LHCb region in Run I [42]. The measured distribution is projected to PLUME geometrical acceptance assuming forward-backward symmetry and scaled by a factor corresponding to an average simulated pile-up value ($\mu = 8$). A ratio of inelastic cross-sections at $\sqrt{s} = 7$ and 13 TeV, $\frac{\sigma_{inel}(\sqrt{s}=13\ TeV)}{\sigma_{inel}(\sqrt{s}=7\ TeV)}$, from Ref. [43], is introduced to account for the evolution of total inelastic cross-section with the center-of-mass energy. The obtained distribution is overlaid in Fig. 29. The occupancy simulated with the chosen PYTHIA version is found to be in a good agreement with the expectations projected from data as described in this paragraph.

Contrary to the ATLAS LUCID detector calibrated with a Bi-207 radioactive source [9], PLUME will use for the calibration the charged particles coming from the IP. In LUCID this was impossible since the signal was dominated by secondaries. At LHCb the coincidence between the two layers should suppress the secondaries roughly by $\sim 1/\text{occupancy} = 1/0.049 \approx 20$ at $\mu = 8$, $z = -1680\,\text{mm}$ and 5.4°. The coincidence is detected in 1.5% of the cases, so the ratio between the primaries and secondaries is approximately $1.5\% : 4.9\% \approx 1 : 3$. According to the simulation, therefore, the coincidence of two PMTs should deliver sufficiently clean signal of particles from the IP, suitable for the PLUME calibration. The purity can be further significantly improved in the offline analysis by requiring that the VELO reconstructed track passed through the PMT.

Simulated signal from pairs of corresponding PMTs in two layers, at $z = -1680\,\text{mm}$ and $-1900\,\text{mm}$, is combined in a logical AND or OR. Figure 30 shows the number of fired channels out of 24 in total per $\mu = 8$ event. The average number of fired PMTs in the first layer (i.e. the average of the "First layer only" spectrum in Fig. 30) is 0.7. The occupancy

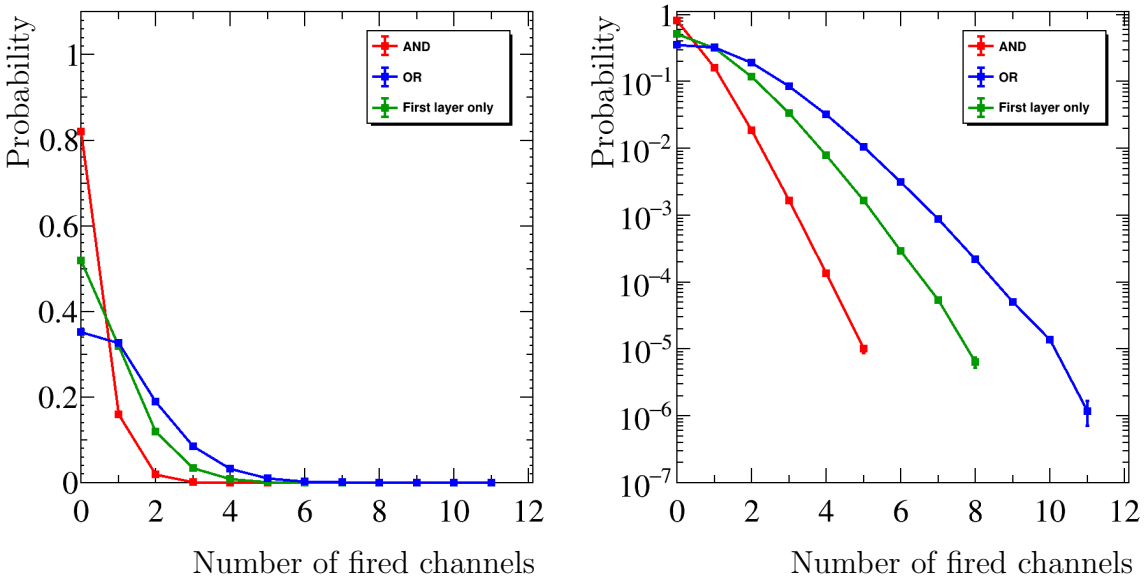

Figure 30: Simulated number of fired channels in the PLUME detector with 24 PMTs in each of the two projective layers. The channel is either a single PMT at $z = -1680\,\text{mm}$ ("First layer only" in the legend) or the logical combination (AND, OR) of a PMT from this layer and a matching PMT at $z = -1900\,\text{mm}$. The pile-up value is $\mu = 8$. Distributions are shown in (left) linear and (right) logarithmic scale for the probability values. All three distributions are normalized to unity.

averaged over these 24 PMTs at various angles with the beam is 0.029. One can see that $0.7 \approx 24 \times 0.029$ which is consistent with the hypothesis of independent firings of PMTs.

In practice, the luminous region extends over several centimetres along the beam axis. Simulations show that there is no significant impact from this on the PLUME occupancies. However, the coverage of the PLUME elementary detectors by the upstream tracks reconstructed in VELO is expected to be improved, which is useful for calibration and monitoring of PLUME.

The activation of the surrounding materials in the bunch crossing N with the delayed decays of excited nuclei in the following bunch crossings $N+1, 2, \ldots$ is potentially dangerous for an accurate luminosity measurement. If PLUME were sensitive to the activation, its measurements would be biased and the required correction would depend on the LHC filling scheme. However, a strong advantage of the Cherenkov detectors, compared to e.g. scintillators, is that they effectively set an energy threshold, since the particles with small velocities do not emit light. This mostly eliminates the sensitivity to the activation. For example, no correction for activation was necessary during the operation of the LUCID detector in ATLAS [9].

8 Luminosity measurements

8.1 Calibration

The LED calibration continuously monitors the PMT responses to a fixed and known amount of light. It will be accurate at least during short periods of the order of fills. The gain and efficiency of the PMTs will vary, but their responses in the number of photons per track from IP will be stabilized and kept approximately constant by adjusting the high voltage and the timing, e.g. after every fill. Because of possible slow ageing of the LED light transportation system or any other relevant deterioration, we can not rely on the LED calibration alone in the longer term. Then, the stability will be ensured using one-track peaks visible in the events with a VELO-reconstructed track passing through a PMT or in a standalone mode using the events with two projective PMTs in the hodoscope above threshold. According to the simulation, one-track peaks will also be visible in this case.

Such VELO-based calibration requires more time and data and can be performed only quasi-online or offline. Ideally, both LED- and VELO-based calibrations will be performed by automatic scripts running e.g. between fills. The calibration can even be performed twice (as is done in LUCID): the first one compensates the ageing while the second one (in ~ 0.5 hour) verifies that the HV adjustment returns the PMT response to the specified constant number of photons per track from IP. Note that in addition to the gain loss due to the ageing, there is a partial recovery during the stops because of annealing.

It is planned to install a few PMTs and accumulate the first experimental spectra during the short run planned at the end of September and beginning of October 2021. Based on the acquired experience, automatic calibration scripts will be developed in 2022.

In principle, the events with the VELO tracks passing through the PLUME PMTs can be accumulated by any HLT line. However, the backgrounds will be different, so it might be useful to compare e.g. two HLT lines with not very "busy" events. Note also that the calibration should be performed with respect to the tracks from IP at $(0, 0, 0)$. The IP (or secondary vertex) displacement from the origin needs to be compensated by the corresponding measured efficiency ratio, which is discussed in Section 8.2.

In addition, the cross-calibrations will be performed with respect to other LHCb detectors that are able to measure luminosity, in particular, those that are based on the number of tracks and vertices reconstructed by the VELO detector.

8.2 Online luminosity measurement

For every PMT and for every bunch-crossing, the TELL40 will accumulate a histogram with two bins: the number of events below and above a threshold. The histograms are reset every few (e.g. three) seconds. All bunch-crossings are counted, including those arriving during the reset.

In addition to individual PMTs, it is planned to accumulate the histograms of coincidences of projective PMTs. This will potentially give better accuracy by reducing the backgrounds and enhancing the contribution from the tracks originating from the interaction region.

Due to the PMT ageing and the background below one-track signal, a special care is required in setting the thresholds. It will be defined with respect to the signal from the

IP tracks. The latter should be kept constant by adjusting the PMT gain and timing, so setting the threshold to a constant value in the electronics will be sufficient. However, programmable threshold values are implemented in the front-end electronics (Section 4.1).

The luminosity at LHC is measured by counting the visible number of interactions per bunch-crossing μ. At LHCb in Run 2, this was determined with the "logZero" method assuming Poisson statistics as

$$\mu = -\log P_0 = -\log \frac{N_0}{N} - \frac{1}{2}\left(\frac{1}{N_0} - \frac{1}{N}\right), \tag{2}$$

where N_0, N are the number of empty and all events, respectively, and P_0 is the fraction of empty events. The definition of the "empty" event depends on the luminometer and means that the detected signal is compatible with zero. For example, for one PLUME PMT N_0 is the number of events with the signal below threshold out of N in total. The second term describes the second-order correction derived in Ref. [46]. Below we present an alternative but equivalent proof.

Let's assume that both μ and N are fixed while the number of empty events n_0 fluctuates around its average value $\langle n_0 \rangle = N_0$ according to a Binomial distribution. Here and in the following the angular brackets denote averaging. Since $e^{-\mu} = P_0 = N_0/N = \langle n_0 \rangle / N$, one has

$$\mu = -\log \frac{\langle n_0 \rangle}{N} \neq -\langle \log \frac{n_0}{N} \rangle$$

due to the non-linearity of the logarithm. The average bias is calculated as

$$\begin{aligned} \mu - \langle -\log \frac{n_0}{N} \rangle &= \langle \log \frac{n_0}{N_0} \rangle = \langle \log \left(1 + \frac{n_0 - N_0}{N_0}\right) \rangle \\ &\approx \langle \frac{n_0 - N_0}{N_0} \rangle - \langle \frac{(n_0 - N_0)^2}{2N_0^2} \rangle. \end{aligned} \tag{3}$$

The mean of the Binomial distribution of n_0 is N_0, so the first term vanishes. The numerator of the second term is the variance of the Binomial distribution $NP_0(1-P_0) = N_0(1-N_0/N)$, so the bias is equal to:

$$\mu - \langle -\log \frac{n_0}{N} \rangle = -\frac{N_0(1 - N_0/N)}{2N_0^2} = -\frac{1}{2}\left(\frac{1}{N_0} - \frac{1}{N}\right), \tag{4}$$

which confirms Eq. 2.

At the 11.245 kHz LHC revolution frequency, in 3 seconds one accumulates $N \approx 33700$ events per bunch crossing. With an example of 1% occupancy this gives $N - N_0 \sim 337$, so that the statistical uncertainties ($\sim 1/\sqrt{N - N_0} \approx 5\%$) per bunch crossing and the second-order correction are small. The statistical uncertainty of the full LHCb luminosity is $5\%/\sqrt{n_{bb}}$, where n_{bb} is the number of colliding bunch pairs, i.e. negligible if $n_{bb} \gg 1$. In 3 s intervals, the value of μ per bunch should be stable and the deviation from the Poisson statistics of Eq. 2 should also be negligible.

The 3564×25 ns bunch slots at LHCb can be classified to 2×2 combinations depending on whether they contain nominal bunches in beam 1 and beam 2. In the following, "beam-beam" denotes the presence of bunches in both beams and thus their collision at LHCb; "beam-empty" and "empty-beam" mean the presence of only the bunch from beam 1 or 2,

respectively, while its counterpart is absent; and in "empty-empty" slots both bunches are absent.

Usually, the physics background is dominated by the beam-gas interactions. These are subtracted using beam-empty (be) and empty-beam (eb) bunch-crossing,

$$\mu = \mu_{bb} - \mu_{be} - \mu_{eb}. \tag{5}$$

This formula is valid only if the bunch populations in the bb, be and eb bunch crossings are similar. The beam-gas background in be and eb bunch crossings is typically small, $\sim$1%, so $\leq 10\%$ difference between the *average* bunch populations in bb, be and eb bunch crossings can be neglected. In case of larger differences, μ_{be} and μ_{eb} in Eq. 5 need to be rescaled according to the measured bunch currents. The background in empty-empty bunch-crossings is usually negligible, but should be monitored for any anomalies.

The histograms and luminosity values per bunch will be archived by the LHCb control system and stored in the online configuration and condition database of the experiment. The advantage of the online measurement is that it is performed with the full available statistics. These histograms will also be used offline after applying efficiency and time drift corrections.

One correction that will be necessary at least in the offline analysis arises from the efficiency dependence on the IP z-position. It will be calibrated using e.g. the calorimeter luminosity measurements during x-y van der Meer (vdM) scans [47] where various IP z-positions are probed due to the beam crossing angle. During the data taking, the IP position is continuously monitored by the VELO detector. This information is available in the experiment control system, so this correction can be performed both offline and online.

The z-correction was sufficient for the luminosity measured with the VELO in Run 1 and Run 2. This is demonstrated in Figs. 31 and 32 for $\sqrt{s} = 13\,\text{TeV}$. Figure 31 shows the efficiency z-dependence for the VELO luminometers based on counting the number of tracks and vertices. Namely, the event is considered empty if it has less than two tracks or one vertex, respectively [3]. The z-dependence is measured via the ratio of $\mu(\text{Track or Vertex})/\mu(\text{SPD} + \text{CaloEt})$, where $\mu(\text{SPD} + \text{CaloEt})$ is determined from the fraction of empty events without sizeable activity in the calorimeters and preshower (SPD). Since they are both located far from the IP and have large acceptance, their efficiencies change negligibly when IP is shifted along z by $O(\text{ cm})$. Therefore, the ratio $\mu(\text{Track or Vertex})/\mu(\text{SPD} + \text{CaloEt})$ is proportional to the efficiencies of the VELO-based luminometers.

Four columns in Fig. 31 are the measurements in vdM scans performed in 2015, 2016, 2017 and 2018. The corresponding LHC fill numbers are shown at the top together with the average z-width of the luminous region. The latter is used for convolving the efficiency with the Gaussian luminous region z-profile. Taking the z-spread σ_z of the IP into account improves the results. The efficiency is parameterized by the 7-th order polynomial. Its parameters, constant across all years, are determined from the simultaneous fits of all scans performed in 2015–2018.

The polynomial convolution with the Gaussian function is conveniently performed using the Gauss-Hermite quadrature. Namely, the convolution is equivalently represented as a linear combination of the polynomial values at 7 fixed points coinciding with the roots of the Hermite polynomial. This reduces potentially complicated fit to a simple linear regression. The calorimeter-based luminometer was not as stable as VELO. Therefore,

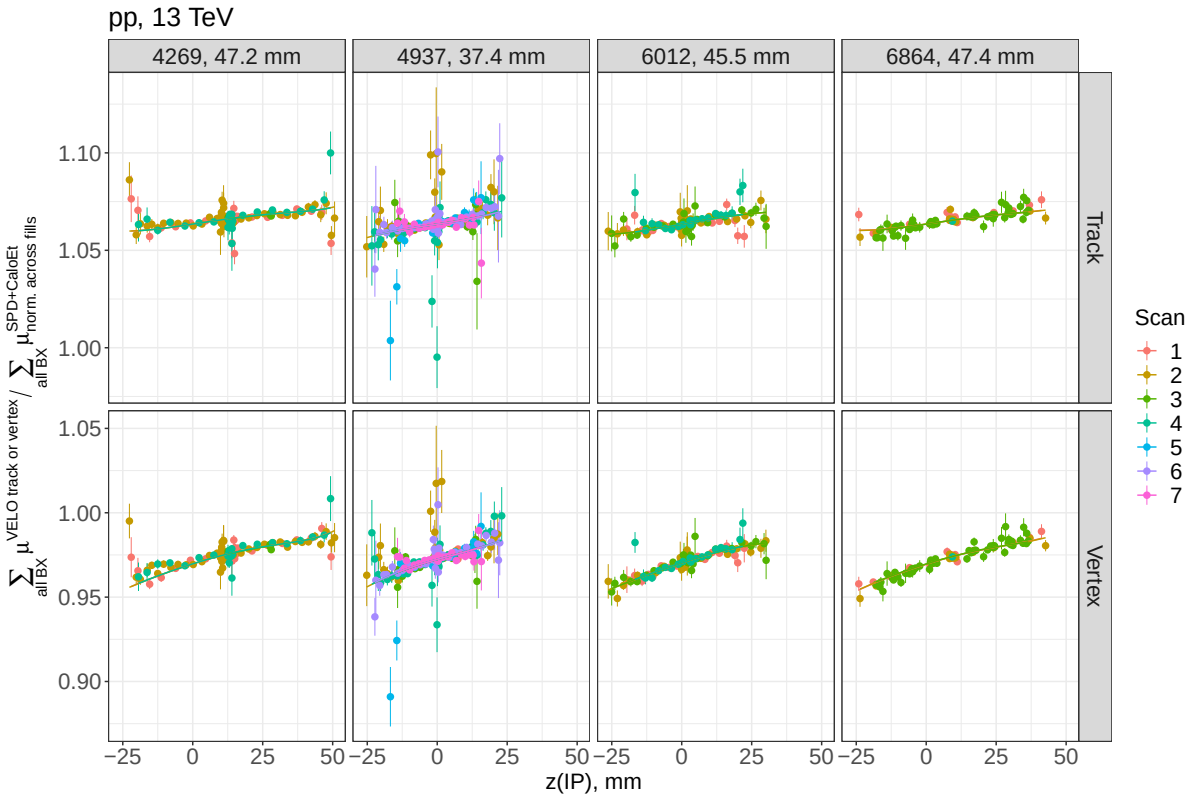

Figure 31: The ratios (top) $\mu(\text{Track})/\mu(\text{SPD}+\text{CaloEt})$ and (bottom) $\mu(\text{Vertex})/\mu(\text{SPD}+\text{CaloEt})$ measured in vdM scans at 13 TeV in 2015, 2016, 2017 and 2018 years (four columns) as a function of the IP z-position. The LHC fill numbers and the average IP z-widths are listed in the top column labels. The curves are the results of the fit described in the text. The colours distinguish vdM scans performed in the same fill.

the absolute normalizations of $\mu(\text{Track or Vertex})/\mu(\text{SPD}+\text{CaloEt})$ ratios in 2016, 2017 and 2018 columns with respect to that in 2015 are free fit parameters. They are found by iterative χ^2 minimization on top of the linear regressions.

The RMS of the luminosity-weighted $z(IP)$ fluctuations in all runs at 13 TeV is ~ 5 mm. This leads to the vertex efficiency variations at the level of $\sim 0.3\%$. The bias of the central value from IP at $z = 0$ with $\sigma_z = 50\,\mu$m, which is the reference in vdM cross-section calibrations, is of the same order.

Figure 32 shows the luminosity-weighted ratio $\mu(\text{Track})/\mu(\text{Vertex})$ across all LHCb runs at 13 TeV. After $z(IP)$ and $\sigma_z(IP)$ corrections, the ratio is stable during four years with RMS of 0.08%. The central value matches the vdM measurement within 0.017%.

If PLUME PMT coincidences will require in addition transverse x, y-corrections or corrections on the beam-crossing angles, they will also be determined during vdM scans and will be monitored during data taking by comparing with the luminometers based on other LHCb subdetectors or with other PLUME PMTs or projective PMT pairs. Due to symmetric placement, a simple averaging over PMTs at the same distance from the beam pipe is expected to already give sufficient accuracy without any further corrections.

The online luminosity will be available for publishing to the LHC beams groups. It will also be integrated to the existing luminosity panel displayed in the control room

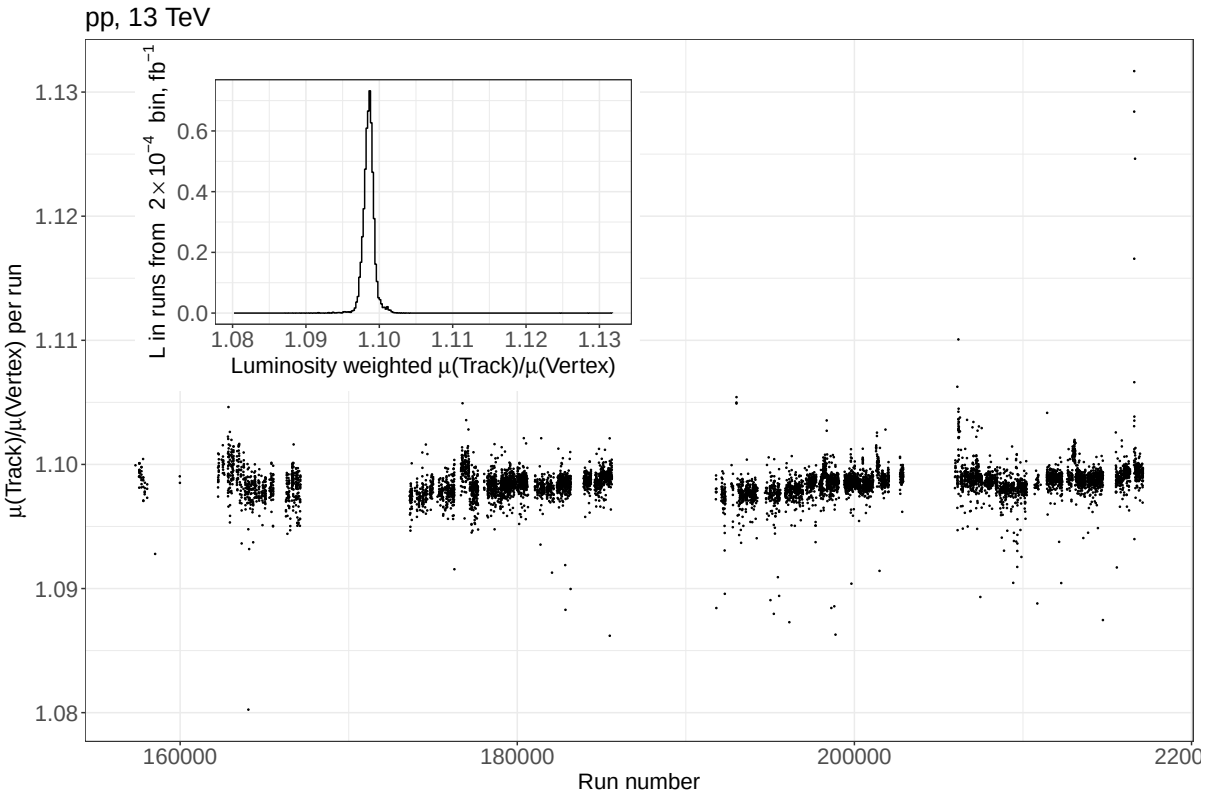

Figure 32: The ratio μ(Track)/μ(Vertex) determined per LHCb run versus the its number for all runs at 13 TeV. The luminosity-weighted projection of this two-dimensional scatter-plot onto a vertical axis is shown in the top-left inset.

for the access of the LHCb shift crew (or a separate panel will be created). The online luminosity value is intended to be used for the LHCb luminosity levelling.

8.3 Offline luminosity

The offline measurement will depend on the HLT and RTA capabilities. Minimally, the PLUME data will be stored in nano-events taken with random triggers. The analysis then proceeds in the same way as outlined above online analysis with, however, significantly reduced event samples.

The advantage, however, is that coincidences not only between matching PLUME hodoscope channels but also with other luminometers can be analysed. Another advantage is that in addition to the "logZero" method described in Eq. 2, one can use the signal amplitudes and the average method. With small occupancies at the level of a few percent, the pile-up probability is small and the analog spectrum above pedestal is dominated by the one-interaction spectrum. The contribution of two interactions is suppressed as $\frac{\mu^2/2}{\mu}$, i.e. as "occupancy"/2. By adjusting the PMT gain and timing, the one-track PMT signal will be kept approximately constant. Small corrections on top of that might be required offline. After that the reconstructed one-interaction spectrum should be constant. This will allow performing a powerful cross-check. Any deviation might reveal some hidden detector effects and systematic uncertainties.

In general, measurements with any single PMT or any pair of projective PMTs are sufficient to measure the luminosity, if free from background and systematic effects. This gives a large redundancy and a possibility of numerous cross-checks. For example, the measured luminosity should be independent of the PMT rapidity value.

If the HLT allows one to store not only per-event information, but also the histograms, one can implement the same histogramming as online, and, possibly, also with the analog spectra in addition to two-bin counters used for the "logZero" method. In this case, the full PLUME information could be used. This might be useful, in particular, for debugging the TELL40 firmware and the implementation of the online luminosity determination there.

9 Detector installation

PLUME detector installation will proceed in two stages. First, a small number (four to six) of elementary detector modules (PLUME phase 1) forming a few hodoscope coincidences will be mounted in July 2021. They will serve to acquire the first experience of PLUME beam operation exploiting the LHC beam circulation during 1-2 weeks and presently planned for the period end of September and beginning of October 2021.

The full PLUME detector installation - PLUME phase 2 - will be mounted in the period December 2021 – January 2022. The elementary detection modules will be assembled and aligned within two respective, A and C, frames. The two equipped frames will be sequentially installed and aligned with respect to the beam axis and the $z = 0$ position using the laser tracker. Then the alignment of elementary detection modules within the frames will be verified. Aligning elementary detector positions with respect to the beam axis to better than 1 mm and aligning the PMT axes with respect to the direction to the nominal collision point to better than 0.05 mrad is foreseen. Due to the installation of pre-assembled detector frames, the installation and alignment will be performed within a short time period. Installation, alignment and connections of the detector in VELO alcove should be accomplished within a time of about one week. Installation and connections of PLUME at the VELO platform (FEE and monitoring system) and in D3 is expected to take more time, two to three weeks. This will be followed by stand-alone checks and commissioning period with short-time accesses required.

The installation and commissioning activity will be coordinated with those by VELO, SMOG2 and BCM as well as with the beam pipe bakeout.

In an unlikely event of urgently required access to the VELO from the upstream direction, the A and C frames of PLUME detector can be disassembled. This procedure will be fast and will take less than one day time. The alignment procedure will have to be repeated after re-installation of PLUME.

10 Operation and maintenance

The detector commissioning will require a presence of key PLUME experts at CERN. Once PLUME is commissioned, a conventional LHCb-style detector operation is expected with a piquet who is able to reach point 8 on a short notice and to contact on-call experts if needed. A similarity of the PLUME electronics to that of the LHCb calorimeter, and the small scale and simplicty of the PLUME detector, suggests that the piquet task may be shared with the calorimeter in the longer term.

An electrical failure or radiation-induced detector degradation can require an access to elementary detectors. While preliminary validation will be performed to prove the reliability of the electrical part of the elementary detectors, GEANT4 simulation and irradiation tests suggest that elementary detectors will survive the radiation dose expected during LHCb Run 3. Despite a small expected failure probability, once the detector is commissioned, an annual replacement of a few elementary detectors is conservatively foreseen for the first year of operation.

The replacement of an elementary detector is possible in an entire block comprising the PMT, voltage divider and a quartz tablet. In order to access the elementary detectors, the corresponding part of the protection grid should be removed. For that the monitoring fiber and the cables should be disconnected and the two corresponding fixations released. The block design of elementary detectors allows a replacement to be time efficient. Due to the radiation level slowly decreasing after the LHC stop, any possible maintenance is preferred to occur during annual LHC winter stop periods.

The number of the PLUME hodoscope channels possesses a sufficient redundancy. This number largely exceeds the number of channels needed to ensure delivering the information for the online luminosity determination and for the luminosity levelling. The offline luminosity analysis profits from the counting of coincidences from the hodoscope detectors symmetric with respect to the beam axis. Therefore, the number of elementary detectors in PLUME assumes the quality of the offline luminosity determination even under a configuration with reduced number of operational channels. In the event of a failure of large number of elementary detectors, which is considered highly improbable, a typically one-hour intervention can allow replacing a significant number of elementary detectors once the access is granted. Spares are foreseen for all components of the PLUME electronics and readout. The TELL40, power rectifiers and remote control components are accessible and can be replaced during the LHC operation, introducing a minimal dead time in the PLUME functioning. A replacement of the components which are located in the detector area, is fast but requires an access.

11 PLUME project planning, organization and cost

Details on the PLUME project are given in this Section. Project planning, organization and cost are discussed.

11.1 Project planning

The PLUME project planning is summarized in Fig. 33 outlining the main steps of design, construction, installation and commissioning of the detector. PLUME Phase 1 (4 to 6 detector modules) will be installed in July 2021. The installation of the detector (referenced as PLUME phase 2) will take place between December 2021 – January 2022. However, a small number of detector channels (referenced as PLUME phase 1) will be installed in July 2021. This will allow a full-scale detector test with the 1-2 weeks long LHC beam circulation planned in September – October 2021.

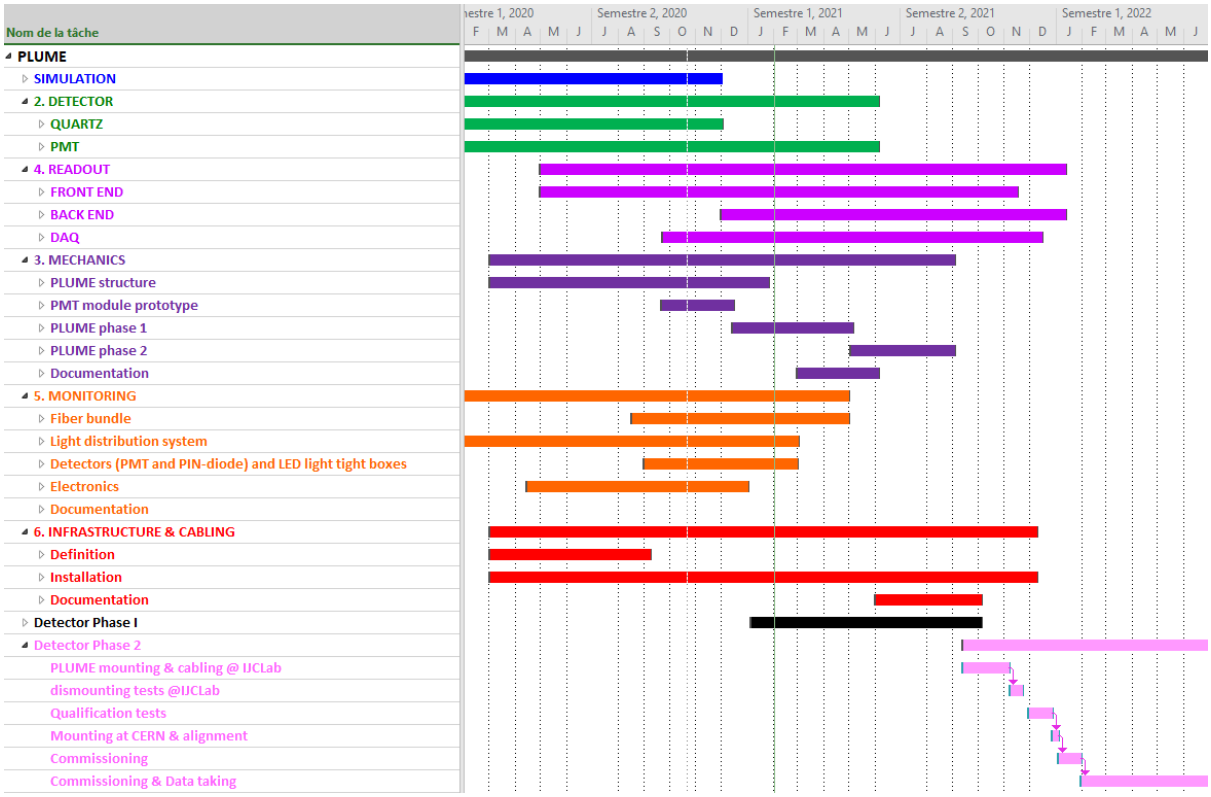

Figure 33: Schematic planning of PLUME project comprising the main steps of design, construction, installation and commissioning.

11.2 Project organization

The PLUME project is developed by the following institutions: CERN-LHCb, EPFL Lausanne, INFN Bologna, IN2P3 IJCLab Orsay and LLR Palaiseau, with contributions from T. Shevchenko National University of Kyiv, Kharkiv ISMA, IHEP Protvino and ITEP Moscow. The project is coordinated by IJCLab Orsay. Table 6 shows the sharing of responsibilities for PLUME project. The institutions listed in the table provide a

Table 6: Sharing of responsibilities for PLUME project.

Task		Institutes
Simulation		Kyiv
Detector	Quartz	Orsay, Kharkiv
	PMT	Bologna, Orsay
	Mechanics	Orsay
Readout	Front-end electronics	Orsay
	Back-end electronics	Bologna
	DAQ	Lausanne
Monitoring		Lausanne
Infrastructure		LHCb, Orsay
Installation and integration		LHCb, Orsay
Luminosity analysis		Palaiseau

dominant contribution and coordinate the corresponding tasks.

11.3 Cost

The estimated PLUME core cost in Swiss francs is detailed in Table 7. An assumed Swiss

Table 7: The PLUME project core cost in units of kCHF.

Task	Cost, kCHF
Mechanics	25
Detector	61
Front-end electronics	13
Back-end electronics and DAQ	14
Monitoring	60
Infrastructure	53
Total	226

francs to Euro exchange rate is 1.07. The estimate is based on the current best knowledge. Due to the limited amount of the core cost, the contingency is not specified. The project is fully funded. Contributions of participating institutions are shown in Table 8.

Table 8: Contributions to the PLUME project core cost in units of kCHF.

Institution	Cost, kCHF
EPFL	60
INFN	27
IN2P3	85
LHCb	53

The annual cost of maintenance and operation will be estimated after the first year of detector operation. It is tentatively expected at the level of 6-7 kCHF.

12 Summary

The PLUME detector is a relatively simple, small and low-cost luminometer for the LHCb detector in Run 3. It relies on registration of Cherenkov light emitted by particles passing through a hodoscope of small quartz-based detectors upstream from the collision region.

The PLUME detector will play an important role in LHCb operation during Run 3. It will deliver the online luminosity and μ measurements for the luminosity levelling; perform these measurements per bunch; measure the radiation background induced by the accelerator or bad vacuum, produce alarms, measure the level of the ghost charges; cross-check the LHC filling scheme in real time; contribute to the centrality determination in the fixed-target program; provide accurate offline luminosity determination.

The performed studies, including simulation, prototype development, test bench and beam tests, and sample irradiation, have shown that the PLUME detector matches the requirements. The studies have demonstrated a feasibility of the detector integration in LHCb, and identified no show-stoppers for the detector construction, installation and commissioning.

A small number of elementary detectors will be installed in July 2021 in order to gain experience with PLUME operation during a planned circulation of the LHC beams in September-October 2021. The remaining detector will be installed during the period December 2021 – January 2022.

Acknowledgements

We express our gratitude to our colleagues in the CERN accelerator departments for the excellent performance of the LHC. We thank the technical and administrative staff at the LHCb institutes. We are greatful to V. Hedberg, B. Giacobbe and W. Kozanecki for useful discussions and sharing their experience of LUCID development and operation. We acknowledge support from CERN and from the national agencies: CAPES, CNPq, FAPERJ and FINEP (Brazil); MOST and NSFC (China); CNRS/IN2P3 (France); BMBF, DFG and MPG (Germany); INFN (Italy); NWO (Netherlands); MNiSW and NCN (Poland); MEN/IFA (Romania); MSHE (Russia); MICINN (Spain); SNSF and SER (Switzerland); NASU (Ukraine); STFC (United Kingdom); DOE NP and NSF (USA). We acknowledge the computing resources that are provided by CERN, IN2P3 (France), KIT and DESY (Germany), INFN (Italy), SURF (Netherlands), PIC (Spain), GridPP (United Kingdom), RRCKI and Yandex LLC (Russia), CSCS (Switzerland), IFIN-HH (Romania), CBPF (Brazil), PL-GRID (Poland) and NERSC (USA). We are indebted to the communities behind the multiple open-source software packages on which we depend. Individual groups or members have received support from ARC and ARDC (Australia); AvH Foundation (Germany); EPLANET, Marie Skłodowska-Curie Actions and ERC (European Union); A*MIDEX, ANR, IPhU and Labex P2IO, and Région Auvergne-Rhône-Alpes (France); IRP/LIA IDEATE (France and Ukraine); Key Research Program of Frontier Sciences of CAS, CAS PIFI, CAS CCEPP, Fundamental Research Funds for the Central Universities, and Sci. & Tech. Program of Guangzhou (China); RFBR, RSF and Yandex LLC (Russia); GVA, XuntaGal and GENCAT (Spain); the Leverhulme Trust, the Royal Society and UKRI (United Kingdom).

References

[1] LHCb collaboration, *Framework TDR for the LHCb Upgrade: Technical Design Report*, CERN-LHCC-2012-007, 2012.

[2] LHCb collaboration, R. Aaij *et al.*, *LHCb detector performance*, Int. J. Mod. Phys. **A30** (2015) 1530022, arXiv:1412.6352.

[3] LHCb collaboration, R. Aaij *et al.*, *Precision luminosity measurements at LHCb*, JINST **9** (2014) P12005, arXiv:1410.0149.

[4] O. Okhrimenko, S. Barsuk, F. Alessio, and V. Pugatch, *LHCb RMS status and operation at 13 TeV*, in *Proceedings of the third French-Ukrainian workshop on the instrumentation developments for HEP*, 61–65, 2015.

[5] V. Talanov *et al.*, *A Beam Loss Scintillator system for background monitoring at the LHCb experiment*, in *Proceedings of the Russian Particle Accelerator Conference (RuPAC)*, 286–288, 2010.

[6] C. Ilgner *et al.*, *The Beam Conditions Monitor of the LHCb experiment*, arXiv:1001.2487.

[7] LHCb collaboration, I. Bediaga *et al.*, *Framework TDR for the LHCb Upgrade: Technical Design Report*, CERN-LHCC-2012-007. LHCb-TDR-12, 2012.

[8] LHCb collaboration, *LHCb SMOG Upgrade*, CERN-LHCC-2019-005, 2019.

[9] G. Avoni *et al.*, *The new LUCID-2 detector for luminosity measurement and monitoring in ATLAS*, JINST **13** (2018) P07017.

[10] M. Karacson, *Evaluation of the radiation environment of the LHCb experiment*, PhD thesis, 2016, https://cds.cern.ch/record/2243499.

[11] V. Balagura *et al.*, *Probe for LUminosity MEasurement in LHCb*, LHCb-PUB-2020-008. CERN-LHCb-PUB-2020-008, CERN, Geneva, 2020.

[12] G. L. Alberghi *et al.*, *Choice and characterization of photomultipliers for the new ATLAS LUCID detector*, JINST **11** (2016) P05014.

[13] V. Cicero, *Neutron radiation resistance of photomultipliers for the LUCID detector in the ATLAS experiment at LHC*, PhD thesis, 2015, https://amslaurea.unibo.it/9410/1/cicero_valentina_tesi.pdf.

[14] SC Secretariat, *Safety Instruction IS 23 (IS 23 Rev. 3)*, BUL-GI-2005-026. 08/2005. 08/2005, 2005.

[15] ATLAS collaboration, C. Sbarra, *The LUCID-2 detector*, Nucl. Instrum. Meth. **A936** (2019) 152.

[16] A. Y. Boyarintsev *et al.*, *Study of radiation-resistant gel bases for composite detectors*, Functional Materials **20** (2013) 471.

[17] A. Y. Boyarintsev *et al.*, *Composite scintillator*, Engineering of Scintillating Materials and Radiation Technologies **200** (2017) 167.

[18] H. Xiao *et al.*, *Optical degradation of polydimethylsiloxane under 150 keV proton exposure*, Journal of Applied Polymer Science **109** (2008) 4060.

[19] M. Phipps, *A New ATLAS ZDC for the High Radiation Environment at the LHC, 18th International Conference on Calorimetry in Particle Physics*, 2018. `http://http://cds.cern.ch/record/2319880`.

[20] V. Puill and others, *PLUME ECR*, EDMS 2432538, 2021.

[21] Y. S. Amhis *et al.*, *The Front-End board of the upgraded LHCb Calorimeter*, LHCb-INT-2019-004. CERN-LHCb-INT-2019-004, CERN, Geneva, 2019.

[22] Y. S. Amhis *et al.*, *3CU Calorimeter Control Card Unit*, LHCb-INT-2019-003. CERN-LHCb-INT-2019-003, CERN, Geneva, 2019.

[23] J. P. Cachemiche *et al.*, *The PCIe-based readout system for the LHCb experiment*, JINST **11** (2016) P02013.

[24] F. Alessio, P. Durante, and G. Vouters, *The readout supervisor firmware for controlling the upgraded LHCb detector and readout system*, `arXiv:1806.08626`.

[25] S. Cap, S. Tjampens and G. Vouters, *LHCb upgrade calorimeter TELL40 data processing*, EDMS 1889215, 2020.

[26] J. Barbosa *et al.*, *Front-end electronics control and monitoring for the LHCb upgrade*, EPJ Web of Conferences **214** (2019) 01002.

[27] I. Guz *et al.*, *Upgrade of the monitoring system of LHCb ECAL*, LHCb-PUB-2016-018. CERN-LHCb-PUB-2016-018, CERN, Geneva, 2016.

[28] A. Konoplyannikov, *Electronics of LHCb calorimeter monitoring system*, in *Proceedings of the Topical Workshop on Electronics for Particle Physics (TWEPP-08), Naxos, Greece, 15-19 Sep 2008*, 397–401, 2008.

[29] R. Martin Lesma *et al.*, *The Versatile Link Demo Board (VLDB)*, JINST **12** (2017) C02020.

[30] A. Arefev *et al.*, *Beam Test Results of the LHCb Electromagnetic Calorimeter.*, LHCb-2007-149. CERN-LHCb-2007-149, CERN, Geneva, 2008. revised version submitted on 2008-05-15 09:09:53.

[31] Y. Guz, A. Konoplyannikov, P. Perret, and P. Shatalov, *Upgrade of the monitoring system of LHCb ECAL*, Nucl. Instrum. Meth. **A912** (2018) 205.

[32] V. B. Gavrilov *et al.*, *Absorption spectra of pure quartz fiber lightguides irradiated with gamma-quanta from a 60 co source*, Instruments and Experimental Techniques **40** (1997) 457.

[33] CMS collaboration, A. Penzo and Y. Onel, *The CMS-HF quartz fiber calorimeters*, J. Phys. Conf. Ser. **160** (2009) 012014.

[34] I. Dumanoglu *et al.*, *Radiation-hardness studies of high OH- content quartz fibres irradiated with 500 MeV electrons*, Nucl. Instrum. Meth. **A490** (2002) 444.

[35] K. Cankoçak *et al.*, *Radiation-hardness measurements of high OH- content quartz fibres irradiated with 24 GeV protons up to 1.25 Grad*, Nucl. Instrum. Meth. **A585** (2008) 20.

[36] F. Duru *et al.*, *Post situ neutron and gamma radiation damage tests on different quartz types*, JINST **11** (2016) T10006.

[37] A. Betata *et al.*, *Calibration and performance of the LHCb calorimeters in Run 1 and 2 at the LHC*, arXiv:2008.11556, 2020.

[38] M. I. Aizatskyi *et al.*, *State and Prospects of the LINAC of Nuclear-Physics Complex with Energy of Electrons up to 100 MeV*, Problems of Atomic Science and Technology, Series: Nuclear Physics Investigations **91** (2014) 60.

[39] CERN Safety Commission, *Revised Safety Instruction 41 (IS41 REV.)*, BUL-GI-2005-216. 48/2005. 49/2005. 48/2005, 2005.

[40] T. Sjostrand, S. Mrenna, and P. Z. Skands, *A Brief Introduction to* PYTHIA *8.1*, Comput. Phys. Commun. **178** (2008) 852, `arXiv:0710.3820`.

[41] J. Allison *et al.*, *Recent developments in* GEANT4, Nucl. Instrum. Meth. **A835** (2016) 186.

[42] LHCb collaboration, R. Aaij *et al.*, *Measurement of charged particle multiplicities and densities in pp collisions at $\sqrt{s}$ =7 TeV in the forward region*, Eur. Phys. J. **C74** (2014) 2888, arXiv:1402.4430.

[43] LHCb collaboration, R. Aaij *et al.*, *Measurement of the inelastic pp cross-section at a centre-of-mass energy of $\sqrt{s}$ =13 TeV*, JHEP **06** (2018) 100, arXiv:1803.10974.

[44] M. Bähr *et al.*, *Herwig++ physics and manual*, Eur. Phys. J. **C58** (2008) 639.

[45] F. W. Bopp, R. Engel, and J. Ranft, *Rapidity gaps and the PHOJET Monte Carlo*, hep-ph/9803437. BA-98-17. SI-98-25, Delaware Univ. Bartol Res. Found. Franklin Inst., Newark, DE, 1998.

[46] M. Schmelling, *Luminosity calibration for the leading bunch nobias-triggered data from the 2015 early measurement runs*, LHCb-INT-2017-015. CERN-LHCb-INT-2017-015, CERN, Geneva, 2017.

[47] S. van der Meer, *Calibration of the effective beam height in the ISR*, CERN-ISR-PO-68-31. ISR-PO-68-31, CERN, Geneva, 1968.